

Dear Dr. Marshall,  
We appreciate very much your comments. Please see our responses below.

*This article documents the land biosphere prior and the optimized land biosphere and ocean posterior fluxes resulting from a 2010-2018 inversion using the Carbon Monitoring System (CMS) modelling system. The observational inputs are restricted to satellite measurements of XCO<sub>2</sub>, based on GOSAT for 2010-2014 and OCO-2 from 2015-2018.*

**Original:** *My first hesitation is based on the appropriateness of publishing optimized fluxes in ESSD. These are not measurements, but rather, by definition, a model-based interpretation of measurements. In the description of the Aims and Scope of the journal it states that: "Any interpretation of data is outside the scope of regular articles." On some level this is a philosophical distinction, and it seems this article has made it through the first quick review process, so I have to assume that the editor does not see a major problem here.*

**Response:** This is a reanalysis dataset, not a pure model simulation. It is a combination of observations and an *a priori* based on their respective error statistics. Reanalysis products have been used more broadly in research than the raw observations. For example, the meteorology reanalysis data sets (e.g., MERRA and ERA-5) have many more users than weather station data or satellite radiances.

**Original:** *My next hesitation is on the criterion of "Completeness". This is one of the categories reviewers are asked to assess, stating that: "A data set or collection must not be split intentionally, for example, to increase the possible number of publications. It should contain all data that can be reviewed without unnecessary increase of workload and can be reused in another context by a reader." The current paper seems to be a classic case of withholding part of the dataset to release it in a future publication. The modelling system used has been well-documented in its ability to (quoting from the Introduction): "resolve regional fluxes, and also disentangle net biosphere exchange (NBE) into constituent carbon fluxes including plant gross primary productivity (GPP) and biomass burning through solar-induced fluorescence and carbon monoxide proxies, respectively (Bowman et al, 2017, Liu et al., 2017)." So is that what is reported here? No, they have decided to only report NBE, stating that "Subsequent papers will present the partitioning of the NBE into constituent gross fluxes." This seems like a clear infringement of the "Completeness" criterion. My recommendation would be to include the optimized GPP, biomass burning, and respiration fluxes in the same data release, and have an accompanying analysis paper (in another journal) that goes into the interpretation of the retrieved signals. One of the unique strengths of the CMS is its partitioning of the net land biosphere fluxes, which most modellers do not claim to be able to do with any confidence. It is this partitioning that would make the resultant fluxes more interesting for comparison against other approaches.*

**Response:** We respectfully disagree that the data are incomplete per ESSD guidance. The NBE can be reviewed independently of component fluxes and can be re-used in many applications by the reader, e.g., comparison to DGVM output, understanding the carbon-climate feedbacks etc. We agree that NBE can be more richly understood by partitioning it into component fluxes. However, there are multiple ways that this can be done, whether through independent data streams or additional data streams (e.g., Liu et al., 2017; Bowman et al., 2017) or through a more sophisticated land-surface assimilation, e.g., Quetin et al, 2020. We do not want to prejudge that methodology or the additional data that might be used.

With respect to NBE, we report all the elements from the inversion system, including gridded fluxes, uncertainties, and regionally aggregated fluxes. We evaluate both the mean fluxes and the uncertainty estimates with independent observations.

We will modify the introduction to reflect the fact that we have not withheld relevant datasets.

G. R. Quetin, A. A. Bloom, K. W. Bowman, A. G. Konings, Carbon Flux Variability From a Relatively Simple Ecosystem Model With Assimilated Data Is Consistent With Terrestrial Biosphere Model Estimates. *J Adv Model Earth Sy.* **12** (2020), doi:10.1029/2019ms001889.

**Original:** *Finally, my third hesitation is related to the data quality. This is not related to anything that the authors themselves have done wrong, but there are (still) clear limitations to using only satellite data in an inversion. This has been well documented in the literature (e.g. Basu et al., 2013; Chevallier et al., 2014), and leads to an unexpectedly high source in northern Africa (and perhaps a too-large sink in Europe) that is hard to reconcile with bottom-up fluxes and inversions based on surface/in-situ measurements. The magnitude of this potential bias has decreased in more recent retrieval versions but has not disappeared. This discrepancy is clearly seen in the limited validation that is presented here, when the optimized concentrations are compared to the Atlantic ATom-1 and -2 flights. At least this inconsistency with independent data is documented: hopefully potential users of this dataset will not assume that their model is wrong simply because it disagrees with the CMS fluxes. One potential improvement here would be to include also fluxes optimized based on surface-based measurements, to give some idea of the uncertainty in the fluxes as a result of the choice of input data. (The estimated fluxes will most likely not agree within the stated uncertainties.) This is downplayed by comparing the global land biosphere budget to widely accepted values from the Global Carbon Project (Friedlingstein et al., 2019), rather than the regional breakdown. Comparing to Figure 8 of Friedlingstein et al. (2019) it seems that the tropics are a more substantial source and the extratropics a more substantial sink than is seen within the spread of inverse models included in the GCP analysis.*

**Response:** We agree with Dr. Marshall that the satellite-based NBE product is not perfect. However, neither is a surface-based inversion product nor is any assimilated product, e.g., ERA5. In particular, surface-based information used in the GCP analysis provides limited information on the tropics. Satellite-based NBE estimates have provided many new insights on the carbon cycle. For example, Basu et al. (2014) studied the flux seasonal variation over tropical Asia with top-down flux estimates based on GOSAT observations. Detmers et al. (2015) studied the 2011 anomalous carbon sink over Australia using NBE estimates based on GOSAT observations. Liu et al. (2018) CMS-Flux results showed excellent agreement with the North American carbon balance changes with in-situ approaches from Wolf et al. (2016). A snapshot of the differences between inversion systems has been documented in Crowell et al. (2019). Those differences will evolve even as a number of these systems converge on their inferences, (e.g., Gaubert et al., 2019). Sharing the data with the broader community will accelerate its use in scientific exploration, and at the same time, will help identify possible deficiencies that further feeds back on future development.

In this paper, we evaluate the reported fluxes and corresponding uncertainties with independent aircraft observations using rigorous methodology. As noticed by Dr. Marshall, we also point to any possible deficiencies in the products based on these evaluations.

Basu, S., Krol, M., Butz, A., Clerbaux, C., Sawa, Y., Machida, T., Matsueda, H., Frankenberg, C., Hasekamp, O. P., and Aben, I. (2014), The seasonal variation of the CO<sub>2</sub> flux over Tropical Asia estimated from GOSAT, CONTRAIL, and IASI, *Geophys. Res. Lett.*, 41, 1809– 1815, doi:[10.1002/2013GL059105](https://doi.org/10.1002/2013GL059105).

Detmers, R. G., Hasekamp, O., Aben, I., Houweling, S., van Leeuwen, T. T., Butz, A., Landgraf, J., Köhler, P., Guanter, L., and Poulter, B. (2015), Anomalous carbon uptake in Australia as seen by GOSAT, *Geophys. Res. Lett.*, 42, 8177– 8184, doi:[10.1002/2015GL065161](https://doi.org/10.1002/2015GL065161).

Crowell, S., Baker, D., Schuh, A., Basu, S., Jacobson, A. R., Chevallier, F., Liu, J., Deng, F., Feng, L., McKain, K., Chatterjee, A., Miller, J. B., Stephens, B. B., Eldering, A., Crisp, D., Schimel, D., Nassar, R., O'Dell, C. W., Oda, T., Sweeney, C., Palmer, P. I., and Jones, D. B. A.: The 2015–2016 carbon cycle as seen from OCO-2 and the global in situ network, *Atmos. Chem. Phys.*, 19, 9797–9831, <https://doi.org/10.5194/acp-19-9797-2019>, 2019.

J. Liu, K. Bowman, N. C. Parazoo, A. A. Bloom, D. Wunch, Z. Jiang, K. R. Gurney, D. Schimel, Detecting drought impact on terrestrial biosphere carbon fluxes over contiguous US with satellite observations. *Environ Res Lett.* **13**, 095003 (2018).

B. Gaubert, B. B. Stephens, S. Basu, F. Chevallier, F. Deng, E. A. Kort, P. K. Patra, W. Peters, C. Rödenbeck, T. Saeki, D. Schimel, I. V. der Laan-Luijkx, S. Wofsy, Y. Yin, Global atmospheric CO<sub>2</sub> inverse models converging on neutral tropical land exchange, but disagreeing on fossil fuel and atmospheric growth rate. *Biogeosciences*. **16**, 117–134 (2019).

S. Wolf, T. F. Keenan, J. B. Fisher, D. D. Baldocchi, A. R. Desai, A. D. Richardson, R. L. Scott, B. E. Law, M. E. Litvak, N. A. Brunsell, W. Peters, and I. T. van der Laan-Luijkx. Warm spring reduced carbon cycle impact of the 2012 US summer drought. *Proceedings of the National Academy of Sciences*, 113(21):5880–5885, 2016. doi: 10.1073/pnas.1519620113. URL <http://www.pnas.org/content/113/21/5880.abstract>.

**Original:** *Another potential limitation to the usefulness of the data is the underwhelming resolution. Monthly fluxes at 4 x 5 degree resolution are no longer really state-of-the-art. One of the arguments for using satellite measurements is the higher spatial resolution of the signals that can be resolved compared to the rather sparse surface-based network. This dataset is not exploiting to this strength.*

**Response:** We chose 4° x 5° to reflect the information content of the current available space-based CO<sub>2</sub> data, rather than an arbitrary grid scale, and we note this spatial resolution has already been scientifically successful (e.g., Liu et al., 2017; Bowman et al., 2017; Liu et al., 2018; Sellers et al., 2018). Before the launch of GOSAT and OCO-2, the tropics had been basically treated as a whole (e.g., Gurney et al., 2002; Baker et al., 2006; Schimel et al., 2015). The 4° x 5° resolution has both scientific value and manageable uncertainties. The estimated posterior flux uncertainty reflects the actual uncertainty as shown in the comparison to aircraft CO<sub>2</sub> observations (Figure 9 in the text). Publishing the dataset will make the dataset easily accessible for more specific regional studies and thus will facilitate rapid progress.

Liu, J., Bowman, K. W., Schimel, D. S., et al. (2017). *Contrasting carbon cycle responses of the tropical continents to the 2015–2016 El Nino*. *Science*, 358 eaam5690.

Sellers, P. J., D. S. Schimel, B. Moore, J. Liu, and A. Eldering, Observing Carbon Cycle-climate feedbacks from space, *Proceedings of the National Academy of Sciences* Jul 2018, 115 (31) 7860–7868; DOI: 10.1073/pnas.1716613115

J. Liu, K. Bowman, N. C. Parazoo, A. A. Bloom, D. Wunch, Z. Jiang, K. R. Gurney, D. Schimel, Detecting drought impact on terrestrial biosphere carbon fluxes over contiguous US with satellite observations. *Environ Res Lett.* **13**, 095003 (2018).

Gurney KR, Law RM, Denning AS *et al.* (2002) Towards robust regional estimates of CO<sub>2</sub> sources and sinks using atmospheric transport models. *Nature*, **415**, 626– 630.

Baker, D. F., et al. (2006), TransCom 3 inversion intercomparison: Impact of transport model errors on the interannual variability of regional CO<sub>2</sub> fluxes, 1988–2003, *Global Biogeochem. Cycles*, 20, GB1002, doi:[10.1029/2004GB002439](https://doi.org/10.1029/2004GB002439).

Schimel D, Stephens BB, Fisher JB. 2015. Effect of increasing CO<sub>2</sub> on the terrestrial carbon cycle. *Proceedings of the National Academy of Sciences, USA* 112: 436–441.

Bowman, K. W., Liu, J., Bloom, A. A., Parazoo, N. C., Lee, M., Jiang, Z., ... Wunch, D. (2017). Global and Brazilian carbon response to El Niño Modoki 2011–2010. *Earth and Space Science*, 4, 637–660. <https://doi.org/10.1002/2016EA000204>

**Original:** *Other comments:*

*Regarding the completeness of the dataset presented, I had some minor concerns. I tried to check the availability of the datasets linked to here, and found that I was not sure which version of the ECCO-Darwin fluxes had been used: the data portal lists several different options. I was not even entirely sure if the ocean fluxes had been optimized, but the netCDF gridded fluxes describe the ocean fluxes as "posterior ocean fluxes, 2010–2014 constrained by GOSAT, 2015–2018 constrained by OCO2", so I assume that they are not identical to the prior. In any case, this could be clarified.*

**Response:** In the revision, we included the prior ocean fluxes, prior biosphere fluxes, and fossil fuel emissions in the gridded product, so the dataset is complete and the readers can calculate carbon budget of any defined region.

**Original:** *Similarly, the paper mentions that FLUXCOM-GPP is one of the inputs to CARDAMOM, but there is more than one version of this product as well. Even CARDAMOM comes in different flavours, I believe, based on the documentation in the cited papers. For completeness it would be suitable to include all the prior and posterior fluxes in the dataset - including the anthropogenic fluxes which are not optimised. Only then can the full budget be assessed.*

**Response:** In the revision, we specified the version of FLUXCOM GPP in the text: “In addition, mean GPP and fire carbon emissions from 2010 - 2017 are constrained by FLUXCOM RS+METEO version 1 GPP (Tramontana et al., 2016; Jung et al., 2017)”.

In the revised dataset, we included all the prior and posterior fluxes in the dataset

**Original:** *I do not see the purpose of providing the monthly fluxes (with uncertainty) at 13 different FLUXNET sites. As far as I can tell, these are extracted directly from the model, and do not represent additional downscaling or enhanced temporal resolution. The benefit of this (and the rationale for the selection of these specific sites) is not clear to me. The measured monthly mean NBE at these sites is not included for comparison, nor is any validation using FLUXNET sites provided in the manuscript. It seems redundant.*

**Response:** We have removed the monthly fluxes at 13 different FLUXNET sites.

**Original:** *I was surprised by the choice of the masks used for aggregation of fluxes. If two masks are included, why not include the broadly-applied TransCom mask? The benefit of such a common mask is the ease of comparison. Yes, a user may apply his or her own mask to the data, but it really does not add much in terms of space (22 regions with monthly resolution), and would facilitate comparison with already available model output. This is likely of more general application than the two custom masks given here.*

**Response:** In the revision, we added the monthly fluxes at TransCom regions (Figures 3, 5, and 8). We revised corresponding text to reflect the changes. In section 4.2, we added the following description: “The availability of flux estimates over the broadly used TransCom regions make it easy to



compare to previous studies. For example, we estimate that the annual net carbon uptake over North America is  $0.7 \pm 0.1$  GtC/year with 0.2 GtC variability between 2010 and 2018, which agrees with  $0.7 \pm 0.5$  GtC/year estimates based on surface CO<sub>2</sub> observations between 1996-2007 (Peylin et al., 2013).” In addition, we revised section 4.4: “We provide the regional mean NBE seasonal cycle, its variability, and uncertainty based on the three regional masks (Table 5). Here we briefly describe the characteristics of the NBE seasonal cycle over the 11 TransCom regions, and its comparison to three independent top-down inversion results based on surface CO<sub>2</sub>, which are CT-Europe (e.g., van der Laan-Luijkx et al., 2017) CAMS (Chevallier et al., 2005), and Jena CarbonScope (Rödenbeck et al., 2003). CMS-Flux-NBE differs the most from surface CO<sub>2</sub>-based inversions over the South American Tropical, Northern Africa, tropical Asia, and NH boreal regions. The CMS-Flux NBE has a larger seasonal cycle amplitude over tropical Asia and Northern Africa, where the surface CO<sub>2</sub> constraint is weak, while it has a smaller seasonal cycle amplitude over the boreal region; this may be due to the sparse satellite observations over the high latitudes and weaker seasonal amplitude of the prior CARDAMOM fluxes. The comparison to FluxSat GPP can only qualitatively evaluate the NBE seasonal cycle, but cannot differentiate among different estimates.”

**Original:** Minor/typographical comments:

L29: “from Greenhouse” -> “from the Greenhouse”

L30: remove “the” before NASA

**Response:** We will correct the grammar.

**Original:** L49: Crowell et al. 2019 is an odd choice as an example of inversions based on surface CO<sub>2</sub> observations, as this was explicitly not the focus of the publication.

**Response:** We replaced the reference with Chevallier et al., 2010.

**Original:** L55: The NBE are far -> NBE is far

L108: suggest “North America (NA)” -> “North American” (abbreviation is established elsewhere, and adjectival form fits better here)

L122: Section 8 is -> Section 8 describes the

L128: “that no” -> “no”

L151: its -> their

L161: from2010 (missing space)

L169: CARDAMON -> CARDAMOM

L184: by ACOS -> by the ACOS

L185: maximize -> maximizes

L193: land nadir good quality observations -> land nadir observations flagged as being of good quality

L221: of OCO-2 -> of the OCO-2

L272: over Pacific, and -> over the Pacific, but

L277: its -> their

L279: each nine -> each of nine

L283: fractions sampled at ith aircraft locations -> fraction sampled at the ith aircraft location

L285: of mean -> of the mean

L287: either posterior fluxes or transport -> either the posterior fluxes or the transport

L288: posterior fluxes -> the posterior fluxes (twice)

L315: of RMSE to posterior flux using GEOS-Chem -> of the RMSE to the posterior flux using the GEOS-Chem  $\hat{A}$

'1

L342: Please rewrite the first sentence.

L355 & L366: by NOAA -> by the NOAA

L360: of posterior -> of the posterior

L371: calculate -> calculated

L375: with GCP -> with the GCP (or, "with the range estimated by the GCP,")

L382: shows large -> shows that large

L382: Southern -> the Southern

L383: eastern -> the eastern

L409: or weakly -> or are weakly

L410: during 2015 -> during the 2015

L415: Pouter -> Poulter

L416: capitalisation weird in "tropical south America Savanna"âˆA

'1

L440: above planetary

-> above the planetary

L446: used NOAA -> used the NOAA

L448: is equal or above -> is greater than or equal toâˆA

'1

L450 & L482 & L497: Southern Ocean -> the Southern Ocean (as an aside: the weaker seasonality certainly plays a role, but this was also a "problem region" in comparison to Atom-1 measurements, so perhaps there is something else going on there: : :)

**Response:** In the revision, we have revised the text accordingly.

**Original::** Figure 2: It is really difficult to tell the regions apart on this map. The blues in North America, for instance, really blend together.

**Response:** We remade Figure 2.

**Original:** Figure 9: This figure seems unnecessarily cramped. Perhaps split it into two? For instance, I could barely tell that the bars were really blue without zooming way in, as they are so tiny.

**Response:** In the revision, we removed the bars, since the number of observations has very little information. We believe that the new figure is clearer.

**Original:** General figure comment: Something is a bit off with the rendering of the digits in your colour bars, making the bottom bar of "2"s disappear and making a gap in the bottom of round digits.

**Response:** we have remade Figures 10 and 11.

**Original:**{ L466: from Monte -> from the Monte

L478: What is meant here? "either transport or low of posterior flux uncertainty estimates": Perhaps, "either transport errors or too low values for posterior flux uncertainties"?

L480: of flight -> of the flight

L493: defined -> as defined

L496: These -> The, also, specify which ratio you mean "between RMSE and RMSEMC"

L500: Pacific -> the Pacific

L503: these -> the

L504: with 4\_x 5\_resolution transport model -> using a transport model with only 4\_x

*5\_resolution*

*L513-515: A bit awkward, please rephrase.*

*L516: indicates small -> indicates a small*

*L518: of posterior -> of the posterior*

*L533: to FLUXSAT -> to the FLUXSAT*

*L541: "needs caution" -> perhaps better: "calls for caution"*

*L556: by GCP -> by the GCP*

*L562: atmospheric -> the atmospheric*

*L563: level -> levels*

*L576: provide support the monitoring of the regional contributions to the changes in atmospheric: : : I'm not sure about this, perhaps: "support the monitoring of the regional (biospheric) contributions to changes in atmospheric: : :"?*

*L580 & L582: data is -> data are*

*L582: ensemble posterior -> ensemble of posterior*

**Response:** We have incorporated all these comments in the revision.

Thanks for the constructive comments. Please see our response below.

Anonymous Referee #2

**Original:** *The authors present a brief description and evaluation results for the inverse model estimated CO<sub>2</sub> fluxes for 2010-2018, based on observations by GOSAT and OCO-2 satellites. The data presented in the dataset are produced with the same model that was applied in several research papers and have mostly been used for estimating the variability and anomalies in the global carbon cycle at the regional and global scale. The satellite-based flux inversions proved to be useful in constraining large regional scale response of the natural carbon cycle to climate anomalies, droughts, heatwaves, such as those driven by the El-Nino cycle. In this context, the presented data can become a useful asset for those studying the carbon cycle variability at regional scale and its connection to the climate anomalies.*

*On the negative side, there are desirable components in the evaluation, such as analysis of the CO<sub>2</sub> flux seasonal cycle, its comparison with inverse model estimates made with ground-based observations, or other independent estimates, such as based on flux tower data. The same can be said on comparison with observed CO<sub>2</sub> concentration at background monitoring sites, such as the NOAA flask sampling network. In case there are identified biases in such comparison, it would be possible to advise the users to restrict the use of the data to studying the flux anomalies rather than using the fluxes for forward simulations, comparing with surface fluxes and using in ecosystem model optimization, where seasonal cycle performance is important. The authors should clearly state such limitations so that the users can have enough information on how to make best use of the provided data. The paper is well written and can be accepted after minor revision addressing the comments and suggestions.*

**Response:** We appreciate the constructive comments. In the revision, we added the comparison to NOAA marine boundary layer reference sites, and compared the seasonal cycle to three publicly available surface CO<sub>2</sub> constrained top-down flux inversions. Please see our detailed response below.

Detailed comments.

**Original:** *Notable deficiency: NBE flux evaluation looks somewhat qualitative. Based on data presented in the paper, and data provided on the data distribution site it is difficult to compare the NBE fluxes to alternative estimates. The 28-region data is provided, but it doesn't look directly mappable to widely used Transcom-3 22 region map. Recommend adding comparison figure (similar to Figure 8) of the seasonal flux climatology on Transcom3 22 regions or the authors-proposed 28 regions to other available estimates such as CAMS inversion fluxes (based on Chevallier et al. 2010) or FLUXCOM fluxes (Jung et al. 2020).*

**Response:** In the revision, we added monthly fluxes at TransCom 3 regions as part of the dataset in addition to the monthly fluxes at the original two regional masks we used in the first version. We revised Figure 3 to include the TransCom 3 region mask, and Figure 5 to include climatological NBE fluxes, variability, and uncertainties at TransCom 3 regions.

We replaced Figure 8 with NBE seasonal cycle comparisons between CMS-Flux NBE and the three publicly available surface CO<sub>2</sub> constrained top-down NBE estimates, which are CAMS, Jena CarbonScope, and CT-Europe. We revised section 4.4 based on the new Figure 8: “We provide the regional mean NBE seasonal cycle, its variability, and uncertainty based on the three regional masks (Table 5). Here we briefly describe the characteristics of the NBE seasonal cycle over the 11 TransCom regions, and its comparison to three independent top-down inversion results based on surface CO<sub>2</sub>, which are CT-Europe (e.g., van der Laan-Luijkx et al., 2017) CAMS (Chevallier et al., 2005), and Jena CarbonScope (Rödenbeck et al., 2003). CMS-Flux-NBE differs the most from surface CO<sub>2</sub>-based inversions over the South American Tropical, Northern Africa, tropical Asia, and NH boreal regions. The CMS-Flux NBE has a larger seasonal cycle amplitude over tropical Asia and Northern

Africa, where the surface CO<sub>2</sub> constraint is weak, while it has a smaller seasonal cycle amplitude over the boreal region; this may be due to the sparse satellite observations over the high latitudes and weaker seasonal amplitude of the prior CARDAMOM fluxes. The comparison to FluxSat GPP can only qualitatively evaluate the NBE seasonal cycle, but cannot differentiate among different estimates. In general, the months that have larger productivity corresponds to months with a net uptake of carbon from the atmosphere, especially over the NH (Figure 8). More research is still needed to understand the seasonal cycles of NBE, including its phase (i.e., transition from source to sink) and amplitude (peak-to-trough difference), and its relationships between GPP and respiration.”

**Original:** Line 208 *It looks like presented bias figures (below 0.1 ppm) are related to global mean bias, are the bias values available as seasonal mean values by latitude or TCCON site? Are retrieved and bias-corrected concentrations consistent with model simulations optimized with ground-based observations?*

**Response:** O’Dell et al. (2018) compared OCO-2 X<sub>CO2</sub> with observations from TCCON sites and the model simulations optimized with ground-based CO<sub>2</sub>. In the revision, we cited O’Dell et al. (2018), and added the following discussion in section 2.3: “O’Dell et al. (2018) showed that the OCO-2 X<sub>CO2</sub> land nadir retrievals has a mean bias ~0.3 ppm and RMS ~1.1 ppm when compared to TCCON retrievals; the differences between OCO-2 X<sub>CO2</sub> retrievals and surface CO<sub>2</sub> constrained model simulations are well within 1.0 ppm over most of the locations in the Northern Hemisphere (NH), where most of the surface CO<sub>2</sub> observations are located.”

O’Dell, C. W., Eldering, A., Wennberg, P. O., Crisp, D., Gunson, M. R., Fisher, B., Frankenberg, C., Kiel, M., Lindqvist, H., Mandrake, L., Merrelli, A., Natraj, V., Nelson, R. R., Osterman, G. B., Payne, V. H., Taylor, T. E., Wunch, D., Drouin, B. J., Oyafo, F., Chang, A., McDuffie, J., Smyth, M., Baker, D. F., Basu, S., Chevallier, F., Crowell, S. M. R., Feng, L., Palmer, P. I., Dubey, M., García, O. E., Griffith, D. W. T., Hase, F., Iraci, L. T., Kivi, R., Morino, I., Notholt, J., Ohyama, H., Petri, C., Roehl, C. M., Sha, M. K., Strong, K., Sussmann, R., Te, Y., Uchino, O., and Velazco, V. A.: Improved retrievals of carbon dioxide from Orbiting Carbon Observatory-2 with the version 8 ACOS algorithm, *Atmos. Meas. Tech.*, 11, 6539–6576, <https://doi.org/10.5194/amt-11-6539-2018>, 2018.

**Original:** Line 1031 *Figure 8. Although the seasonally varying fluxes look to be in a reasonable range it is very much advisable to compare/plot along with observed or observation-based fluxes, such as FLUXCOM NEE product (Jung et al. 2020).*

**Response:** See our response above.

Technical corrections.

**Original:** Line 191 *Looks anomalous, to have 2000 good quality retrievals available on a single day in the ACOS-GOSAT dataset (appears significantly larger than average).*

**Response:** The number 2000 is the number of soundings that are processed by retrieval algorithm, not the number of good quality observations. The number of good quality retrievals is between ~100-300 daily.

**Original:** Line 193 *Need to state how good quality is defined (what value of the quality flag is used)?*

**Response:** We clarified in the revision: “We only assimilate ACOS-GOSAT land nadir good quality observations, which are the retrievals with quality flag equal to 1.”

**Original:** Line 199 *Is ‘super observations’ a good term to name 100 km (\_12 sec) average data?*

**Response:** This term was originated from numerical weather prediction. In the revision, we cited a relevant reference to further clarify the term: “To reduce the sampling error due to the resolution differences between the transport model and OCO-2 observations, we generate super observations by aggregating the observations within ~100 km (along the same orbit) (Liu et al., 2017). The super-obbing strategy was first proposed in numerical weather prediction (NWP) to assimilate dense observations (Lorenc, 1981), and is still broadly used in NWP (e.g., Liu and Rabier, 2003).”

**Original:** Line 228 *The statement “For large-order systems, the posterior errors cannot be explicitly calculated” can be argued. Posterior flux uncertainty projected to regions can be estimated analytically using recipes provided by (Fisher and Courtier, 1995) or (Meirink et al, 2008), using either flux singular vectors or flux increments obtained on course of the iterative optimization (eg Niwa and Fujii, 2020). Using random perturbations is simpler and is used widely, but that doesn’t mean that the more accurate method is impossible to apply.*

**Response:** In section 2.4, we incorporated the above comments when we discuss the posterior flux uncertainty estimation: “Posterior flux uncertainty projected to regions can be estimated analytically based on the methods described in Fisher and Courtier (1995) or Meirink et al. (2008), using either flux singular vectors or flux increments obtained during the iterative optimization (e.g., Niwa and Fujii, 2020). In this study, we rely on a Monte Carlo approach to quantify posterior flux uncertainties following Chevallier et al. (2010) and Liu et al. (2014), which is simpler and widely used.”

**Original:** Line 240 *Common perception is that tower footprint size is less than 1 km, based on estimates by Baldocchi, (1997) and others. The citation by Running et al (1999) of ‘several km<sup>2</sup>’ may refer to the upper range. They (Running et al 1999) also consider 1–3 km<sup>2</sup> and 1 km<sup>2</sup> as typical values throughout their paper.*

**Response:** We revised the description to: “Direct NBE estimates from flux towers only provide a spatial representation of roughly 1 – 3 kilometers (Running et al., 1999),...”





## Carbon Monitoring System Flux Net Biosphere Exchange 2020 (CMS-Flux NBE 2020)

Junjie Liu<sup>1,2\*</sup>, Latha Baskaran<sup>1</sup>, Kevin Bowman<sup>1</sup>, David S. Schimel<sup>1</sup>, A. Anthony Bloom<sup>1</sup>, Nicholas C. Parazoo<sup>1</sup>, Tomohiro Oda<sup>3,4</sup>, Dustin Carroll<sup>5</sup>, Dimitris Menemenlis<sup>1</sup>, Joanna Joiner<sup>6</sup>, Roisin Commane<sup>7</sup>, Bruce Daube<sup>8</sup>, Lucianna V. Gatti<sup>9</sup>, Kathryn McKain<sup>10,11</sup>, John Miller<sup>10</sup>, Britton B. Stephens<sup>12</sup>, Colm Sweeney<sup>10</sup>, Steven Wofsy<sup>8</sup>,

1. Jet Propulsion Laboratory, Caltech, CA
2. Caltech, CA
3. Global Modeling and Assimilation Office, NASA Goddard Space Flight Center
4. Goddard Earth Sciences Technology and Research, Universities Space Research Association, Columbia, MD
5. Moss Landing Marine Laboratories, San José State University, California, CA
6. Laboratory for Atmospheric Chemistry and Dynamics, NASA Goddard Space Flight Center
7. Lamont-Doherty Earth Observatory of Columbia University, NY
8. Harvard University, Cambridge, MA
9. LaGEE, CCST, INPE- National Institute for Space Research, Brazil
10. NOAA, Global Monitoring Laboratory, Boulder, CO 80305
11. University of Colorado, Cooperative Institute for Research in Environmental Sciences, Boulder, CO
11. National Center for Atmospheric Research, Boulder, CO 80301

Correspondence: Junjie Liu (junjie.liu@jpl.nasa.gov)

**Abstract.** Here we present a global and regionally-resolved terrestrial net biosphere exchange (NBE) dataset with corresponding uncertainties between 2010–2018: CMS-Flux NBE 2020. It is estimated using the NASA Carbon Monitoring System Flux (CMS-Flux) top-down flux inversion system that assimilates column CO<sub>2</sub> observations from the Greenhouse gases Observing SATellite (GOSAT) and the NASA's Observing Carbon Observatory -2 (OCO-2). The regional monthly fluxes are readily accessible as tabular files, and the gridded fluxes are available in NetCDF format. The fluxes and their uncertainties are evaluated by extensively comparing the posterior CO<sub>2</sub> mole fractions with CO<sub>2</sub> observations from aircraft and the NOAA marine boundary layer reference sites. We describe the characteristics of the dataset as global total, regional climatological mean, and regional annual fluxes and seasonal cycles. We find that the global total fluxes of the dataset agree with atmospheric CO<sub>2</sub> growth observed by the surface-observation network within uncertainty. Averaged between 2010 and 2018, the tropical regions range from close-to neutral in tropical South America to a net source in Africa; these contrast with the extra-tropics, which are a net sink of  $2.5 \pm 0.3$  gigaton carbon per year. The regional satellite-constrained NBE estimates provide a unique perspective for understanding the terrestrial biosphere carbon dynamics and monitoring changes in regional contributions to the changes of atmospheric CO<sub>2</sub> growth rate. The gridded and regional aggregated dataset can be accessed at: <https://doi.org/10.25966/4v02-c391> (Liu et al., 2020).

Deleted: Carroll<sup>5</sup>

Deleted: Joiner<sup>3</sup>

Deleted: Commane<sup>6</sup>

Deleted: Daube<sup>7</sup>

Deleted: Gatti<sup>8</sup>

Deleted: McKain<sup>9</sup>

Deleted: <sup>10</sup>

Deleted: Miller<sup>9</sup>

Deleted: Stephens<sup>11</sup>

Deleted: Sweeney<sup>9</sup>

Deleted: Wofsy<sup>7</sup>

Deleted: <#>Global Modeling and Assimilation Office, NASA Goddard Space Flight Center, Greenbelt, MD

Moved (insertion) [4]

Deleted: ¶

Formatted: Normal (Web), Indent: First line: 0"

Moved up [4]: <#>Moss Landing Marine Laboratories, San José State University, California, CA

Deleted: the

Deleted: uncertainty

Deleted: estimates

Deleted: CO<sub>2</sub> observations

## Introduction

New “top-down” inversion frameworks that harness satellite observations provide an important complement to global aggregated fluxes (e.g., Global Carbon Project, Friedlingstein et al., 2019) and inversions based on surface CO<sub>2</sub> observations (e.g., Chevallier et al., 2010), especially over the tropics and the Southern Hemisphere (SH) where conventional surface CO<sub>2</sub> observations are sparse. The net biosphere exchange (NBE) is far more variable than ocean fluxes (Lovenduski and Bonan, 2017) or fossil fuel emissions (Yin et al, 2019), and is thus the focus of this dataset estimated from a top-down atmospheric CO<sub>2</sub> inversion of satellite column CO<sub>2</sub> dry-air mole fraction (X<sub>CO<sub>2</sub></sub>). Here, we present the global and regional NBE as a series of maps, time series and tables, and disseminate it as a public dataset for further analysis and comparison to other sources of flux information. The gridded NBE dataset and its uncertainty, air-sea fluxes, and fossil fuel emissions are also available, so that users can calculate carbon budget from regional to global scale. The NBE can be subsequently decomposed into individual fluxes using ancillary measurements (i.e., gross primary production (GPP), respiration, fires, fossil fuel, etc.) to provide process understanding on regional carbon flux variability (e.g., Liu et al., 2017; Bowman et al., 2017). Finally, we provide a comprehensive evaluation of both mean and uncertainty estimates against the CO<sub>2</sub> observations from independent airborne datasets and the NOAA marine boundary layer (MBL) reference sites (Conway et al., 1994).

Global top-down atmospheric CO<sub>2</sub> flux inversions have been historically used to estimate regional terrestrial NBE, which is the net carbon flux of all the land-atmosphere exchange processes except fossil fuel emissions. They make use of the spatiotemporal variability of atmospheric CO<sub>2</sub>, which is dominated by NBE, to infer net carbon exchange at the surface (Chevallier et al., 2005; Baker

Deleted: .....Page Break.....

Deleted:

Deleted: Crowell et al., 2019

Deleted: .

Deleted: These satellite-constrained estimates resolve regional fluxes, and also disentangle net biosphere exchange (NBE) into constituent carbon fluxes including plant gross primary productivity (GPP) and biomass burning through solar-induced fluorescence and carbon monoxide proxies, respectively (Bowman et al, 2017, Liu et al., 2017). Both the spatial and process resolution are critical for evaluating models and reducing uncertainties about future carbon-climate feedbacks (e.g., Friedlingstein et al., 2014).

Deleted: NBE

Deleted: are

Deleted: are

Deleted:

Deleted: W

Deleted: dataset

Formatted: Subscript

Deleted: an

Deleted: Subsequent papers will present the partitioning of the NBE into constituent gross fluxes.

Deleted: ¶

Deleted: is a sum of net ecosystem exchange and biomass burning carbon fluxes

116 et al., 2006; Liu et al., 2014). The accuracy of the NBE from top-down flux inversion is determined  
117 by the density and accuracy of the CO<sub>2</sub> observations, the accuracy of modeled atmospheric  
118 transport, and knowledge of the prior uncertainties of the flux inventories.

119

120 For CO<sub>2</sub> flux inversions based on high precision *in situ* and flask observations, the measurement  
121 error is low (<0.2 parts per million (ppm)) and not a significant source of error; however, these  
122 observations are limited spatially, and are concentrating primarily over North America (NA) and  
123 Europe (Crowell et al., 2019). Satellite X<sub>CO<sub>2</sub></sub> from CO<sub>2</sub>-dedicated satellites, such as the Greenhouse  
124 Gases Observing Satellite (GOSAT) (launched in July 2009) and the Observing Carbon  
125 Observatory 2 (OCO-2) (Crisp et al., 2017) have much broader spatial coverage (O'Dell et al.,

126 2018), [which](#) fill the observational gaps of conventional surface CO<sub>2</sub> observations, but they have  
127 up to an order of magnitude higher single-sounding uncertainty and potential systematic errors  
128 compared to the *in situ* and flask CO<sub>2</sub> observations. Recent progress in instrument error  
129 characterization, spectroscopy, and retrieval methods have significantly improved the accuracy  
130 and precision of the X<sub>CO<sub>2</sub></sub> retrievals (O'Dell et al., 2018; Kiel et al., 2019). The single sounding  
131 random error of X<sub>CO<sub>2</sub></sub> from OCO-2 is ~1.0 ppm (Kulawik et al., 2019). A recent study by Byrne et  
132 al. (2020) shows less than a 0.5 ppm difference between posterior X<sub>CO<sub>2</sub></sub> constrained by a recent  
133 data set, ACOS-GOSAT b7 X<sub>CO<sub>2</sub></sub> retrievals, and those constrained by conventional surface CO<sub>2</sub>  
134 observations. Chevallier et al. (2019) also showed that OCO-2 based flux inversion had similar  
135 performance to surface CO<sub>2</sub> based flux inversions when comparing posterior CO<sub>2</sub> mole fractions  
136 to aircraft CO<sub>2</sub> in the free troposphere. Results from these studies show that systematic  
137 uncertainties in CO<sub>2</sub> retrievals from satellites are comparable to, or smaller than, other uncertainty  
138 sources in atmospheric inversions (e.g. transport).

Deleted: and

140

141 A newly-developed biogeochemical model-data fusion system, CARDAMOM, made progress in  
142 producing NBE uncertainties, along with mean values that are consistent with a variety of  
143 observations assimilated through a Markov Chain Monte Carlo (MCMC) method (Bloom et al.,  
144 2016; 2020). Transport model errors in general have also been reduced relative to earlier transport  
145 model intercomparison efforts, such as [TransCom 3](#) (Gurney et al., 2004; Gaubert et al., 2019).  
146 Advancements in satellite retrieval, transport, and prior terrestrial biosphere modeling have led to  
147 more mature inversions constrained by satellite  $X_{CO_2}$  observations.

148

149 Two satellites, GOSAT and OCO-2, have now produced more than 10 years of observations. Here  
150 we harness the CMS-Flux inversion framework (Liu et al., 2014; 2017; 2018; Bowman et al., 2017)  
151 to generate an NBE product: CMS-Flux NBE 2020, by assimilating both GOSAT and OCO-2 from  
152 2010–2018. The dataset is the longest satellite-constrained NBE product so far. The CMS-Flux  
153 framework exploits globally available  $X_{CO_2}$  to infer spatially-resolved total surface-atmosphere  
154 exchange. [In combination with constituent fluxes, e.g., GPP, NBE from](#) CMS-Flux framework  
155 have been used to assess the impacts of El Niño on terrestrial biosphere fluxes (Bowman et al.,  
156 2017; Liu et al, 2017) and the role of droughts in the North American [carbon balance](#) (Liu et al,  
157 2018). These fluxes have furthermore been ingested into land-surface data assimilation systems to  
158 quantify heterotrophic respiration (Konings et al., 2019), evaluate structural and parametric  
159 uncertainty in carbon-climate models (Quetin et al., 2020), and inform climate dynamics (Bloom  
160 et al., 2020). We present the regional NBE and its uncertainty based on [three](#) types of regional  
161 masks: (1) latitude and continent, [2\) distribution of biome types \(defined by plant functional types\),](#)  
162 and continent, [and 3\) TransCom regions \(Gurney et al., 2004\).](#)

Deleted: TRANSCOM

Deleted: , which can be subsequently decomposed into individual fluxes using ancillary measurements (i.e., GPP, respiration, fires, fossil fuel, etc.)

Deleted: The flux estimates from the

Deleted: (NA)

Deleted: two

Deleted: ;

Deleted: and )

Deleted: .

Deleted: The gridded NBE dataset and its uncertainty are also available, so that users can aggregate the fluxes and uncertainties based on self-defined regions.

176

177 The outline of the paper is as follows: Section 2 describes methods, and Sections 3 and 4 describe  
178 the dataset and the major NBE characteristics, respectively. We extensively evaluate the posterior  
179 fluxes and uncertainties by comparing the posterior CO<sub>2</sub> mole fractions against aircraft  
180 observations and the NOAA MBL reference CO<sub>2</sub> and a gross primary production (GPP) product  
181 (section 5). In Section 6, we discuss the strength and weakness, and potential usage of the data. A  
182 summary is provided in Section 7, and Section 8 describes the dataset availability and future plan.

183

## 184 2 Methods

### 185 2.1 CMS-Flux inversion system

186 The CMS-Flux framework is summarized in Figure 1. The center of the system is the CMS-Flux  
187 inversion system, which optimizes NBE and air-sea net carbon exchanges with a 4D-Var inversion  
188 system (Liu et al., 2014). In the current system, we assume no uncertainty in fossil fuel emissions,  
189 which is a widely adopted assumption in global flux inversion systems (e.g., Crowell et al., 2019),  
190 since the uncertainty in fossil fuel emissions at regional scales is substantially less than the NBE  
191 uncertainties. The 4D-Var minimizes a cost function that includes two terms:

$$192 J(\mathbf{x}) = (\mathbf{x} - \mathbf{x}_b)^T \mathbf{B}^{-1} (\mathbf{x} - \mathbf{x}_b) + (\mathbf{y} - h(\mathbf{x}))^T \mathbf{R}^{-1} (\mathbf{y} - h(\mathbf{x})) \quad (1)$$

193 The first term measures the differences between the optimized fluxes and the prior fluxes  
194 normalized by the prior flux error covariance  $\mathbf{B}$ . The second term measures the differences between  
195 observations ( $\mathbf{y}$ ) and the corresponding model simulations ( $h(\mathbf{x})$ ) normalized by the observation  
196 error covariance  $\mathbf{R}$ . The term  $h(\cdot)$  is the observation operator that calculates observation-  
197 equivalent model-simulated  $X_{\text{CO}_2}$ . The 4D-Var uses the adjoint (i.e., the backward integration of  
198 the transport model) (Henze et al., 2004) of the GEOS-Chem transport model to calculate the

Formatted: Subscript

Deleted: observations

Deleted: and

Deleted: is

Deleted: that

Moved (insertion) [1]

Deleted: .

Deleted: ,

Moved up [1]: which is a widely adopted assumption in global flux inversion systems (e.g., Crowell et al., 2019).

Deleted: include

Deleted: the sum of

Field Code Changed

Deleted: , and

Deleted: t

Deleted: simulated value

Field Code Changed

Field Code Changed



212 sensitivity of the observations to surface fluxes. The configurations of the inversion system are  
213 summarized in Table 1. We run both the forward and adjoint at 4° x 5° spatial resolution, and  
214 optimize monthly NBE and air-sea carbon fluxes at each grid point from January 2010 to  
215 December 2018. Inputs for the system include prior carbon fluxes, meteorological drivers, and the  
216 satellite  $X_{CO_2}$  (Figure 1). Section 2.2 (Table 2) describes the prior flux and its uncertainties, and  
217 section 2.3 (Table 3) describes the observations and the corresponding uncertainties.

218

## 219 2.2 The prior CO<sub>2</sub> fluxes and uncertainties

220 The prior CO<sub>2</sub> fluxes include NBE, air-sea carbon exchange, and fossil fuel emissions (see Table  
221 2). The data sources for the prior fluxes are listed in Table 7 and provided in the gridded fluxes.  
222 Methods to generate prior ocean carbon fluxes and fossil fuel emissions are documented in Brix  
223 et al., (2015), Caroll et al. (2020), and Oda et al. (2018). The focus of this dataset is optimized  
224 terrestrial biosphere fluxes, so we briefly describe the prior terrestrial biosphere fluxes and its  
225 uncertainties.

226

227 We construct the NBE prior using the CARDAMOM framework (Bloom et al., 2016).  
228 CARDAMOM data assimilation system explicitly represents the time-resolved uncertainties in the  
229 NBE. The prior estimates are already constrained with multiple data streams accounting for  
230 measurement uncertainties following a similar Bayesian approach used in the 4D-variational  
231 approach. We use the CARDAMOM setup as described by Bloom et al. (2016, 2020) resolved at  
232 monthly timescales; data constraints include GOME-2 solar-induced fluorescence (Joiner et al.,  
233 2013), MODIS Leaf Area Index (LAI), and biomass and soil carbon (details on the data  
234 assimilation are provided in Bloom et al. (2020)). In addition, mean GPP and fire carbon emissions

Deleted: P

Deleted: net carbon fluxes

from 2010 - 2017 are constrained by FLUXCOM GPP (Tramontana et al., 2016) and GFEDv4.1s (Randerson et al., 2018), respectively, both assimilated with an uncertainty of 20%. We use the Olsen and Randerson (2001) approach to downscale monthly GPP and respiration fluxes to 3-hourly timescales, based on ERA-interim re-analysis of global radiation and surface temperature. Fire fluxes are downscaled using the GFEDv4.1 daily and diurnal scale factors on monthly emissions (Giglio et al., 2013). Posterior CARDAMOM NBE estimates are then summarized as NBE mean and standard deviation values.

The NBE from CARDAMOM shows net carbon uptake of 2.3 GtC/year over the tropics and close to neutral in the extratropics (Figure S1). The year-to-year variability (i.e., interannual variability, IAV) estimated from CARDAMOM from 2010–2017 is generally less than 0.1 gC/m<sup>2</sup>/day outside of the tropics (Figure S1). Because of the weak interannual variability estimated by CARDAMOM, we use the same 2017 NBE prior for 2018.

CARDAMOM generates uncertainty along with the mean state. The relative uncertainty over the tropics is generally larger than 100%, and the magnitude is between 50% and 100% over the extratropics (Figure S2). We assume no correlation in prior flux errors in either space or time. The temporal and spatial error correlation estimates can in principle be computed by CARDAMOM. We anticipate incorporating these error correlations in subsequent versions of this dataset.

### 2.3 Column CO<sub>2</sub> observations from GOSAT and OCO-2

We use satellite-column CO<sub>2</sub> retrievals from Atmospheric Carbon Observations from Space (ACOS) team for both GOSAT (version 7.3) and OCO-2 (version 9) (Table 3). The use of the same retrieval algorithm and validation strategy adopted by the ACOS team to process both

Deleted: N

Deleted: T

263 GOSAT and OCO-2 spectra maximizes the consistency between these two datasets. Both GOSAT  
 264 and OCO-2 satellites carry high-resolution spectrometers optimized to return high precision  
 265 measurements of reflected sunlight within CO<sub>2</sub> and O<sub>2</sub> absorption bands in the shortwave infrared  
 266 (Crisp et al., 2012). Both satellites fly in a sun-synchronous orbit. GOSAT has a 13:00 ± 0.15  
 267 hours local passing time and a three-day ground track repeat cycle. The footprint of GOSAT is  
 268 ~10.5 km in diameter in sun-nadir view (Crisp et al., 2012). The daily number of soundings  
 269 processed by the ACOS-GOSAT retrieval algorithm is between a few hundreds to ~2000. Further  
 270 quality control and filtering reduce the ACOS-GOSAT X<sub>CO2</sub> retrievals to ~100 – 300 daily (Figure  
 271 S5 in Liu et al., 2017). We only assimilate ACOS-GOSAT land nadir observations flagged as  
 272 being good quality, which are the retrievals with quality flag equal to zero.  
 273  
 274 OCO-2 has a 13:30 local passing time and 16-day ground track repeat cycle. The nominal  
 275 footprints of the OCO-2 are 1.25 km wide and ~2.4 km along the orbit. Because of their small  
 276 footprints and sampling strategy, OCO-2 has many more X<sub>CO2</sub> retrievals than ACOS-GOSAT. To  
 277 reduce the sampling error due to the resolution differences between the transport model and OCO-  
 278 2 observations, we generate super observations by aggregating the observations within ~100 km  
 279 (along the same orbit) (Liu et al., 2017). The super-obsing strategy was first proposed in numerical  
 280 weather prediction (NWP) to assimilate dense observations (Lorenc, 1981), and is still broadly  
 281 used in NWP (e.g., Liu and Rabier, 2003). More detailed information about OCO-2 super  
 282 observations can be found in Liu et al. (2017). OCO-2 has four observing modes: land nadir, land  
 283 glint, ocean glint, and target. Following Liu et al. (2017), we only use land nadir observations. The  
 284 super observations have more uniform spatial coverage and are more comparable to the spatial

Deleted: cro

Deleted: observations

Deleted: .

Deleted: crossing

Deleted: its

Moved (insertion) [2]

Deleted: from OCO-2 to generate a set of super observations by aggregating the observations within ~100 km (along the same orbit).

293 representation of ACOS-GOSAT observations [and the transport model](#) (see Figure S5 in Liu et al.,  
294 2017).

295

296 We directly use observational uncertainty provided with ACOS-GOSAT b7.3 to represent the  
297 observation error [statistics](#),  $\mathbf{R}$ , in Eq 1. The uncertainty of the OCO-2 super observations is the  
298 sum of the variability of  $X_{\text{CO}_2}$  used to generate each individual super observation and the mean  
299 uncertainty provided in the original OCO-2 retrievals. Kulawik et al. (2019) showed that both  
300 OCO-2 and ACOS-GOSAT bias-corrected retrievals have [a mean bias of -0.1 ppm when compared](#)  
301 [with  \$X\_{\text{CO}\_2}\$  from Total Carbon Column Observing Network \(TCCON\) \(Wunch et al., 2011\),](#)  
302 indicating consistency between ACOS-GOSAT and OCO-2 retrievals. [O'Dell et al. \(2018\) showed](#)  
303 [that the OCO-2  \$X\_{\text{CO}\_2}\$  land nadir retrievals has RMS error of ~1.1 ppm when compared to TCCON](#)  
304 [retrievals; the differences between OCO-2  \$X\_{\text{CO}\_2}\$  retrievals and surface  \$\text{CO}\_2\$  constrained model](#)  
305 [simulations are well within 1.0 ppm over most of the locations in the Northern Hemisphere \(NH\),](#)  
306 [where most of the surface  \$\text{CO}\_2\$  observations are located.](#)

307

308 The magnitude of observation errors used in  $\mathbf{R}$  is generally above 1.0 ppm, larger than the sum of  
309 random error and biases in the observations. The ACOS-GOSAT b7.3 observations from July  
310 2009–June 2015 are used to optimize fluxes between 2010 and 2014, and the OCO-2  $X_{\text{CO}_2}$   
311 observations from Sep 2014–June 2019 are used to optimize fluxes between 2015 and 2018.

312

313 The observational coverage of ACOS-GOSAT and OCO-2 is spatiotemporally dependent, with  
314 more coverage during summer than winter over the NH, and more observations over mid-latitudes  
315 than over the tropics (Figure S3). The variability (i.e., standard deviation) of annual total number

Moved up [2]: More detailed information about OCO-2 super observations can be found in Liu et al. (2017).

Deleted: es

Deleted: against

Formatted: Subscript

Formatted: Subscript

Formatted: Subscript

320 of observations from 2010–2014 is within 4% of the annual mean number for ACOS-GOSAT.  
321 Except for a data gap in 2017 caused by a malfunction of OCO-2 instrument, the variability of  
322 annual total number of observations between 2015 and 2018 is within 8% of the annual mean  
323 number for OCO-2.

324

## 325 2.4 Uncertainty quantification

326 The posterior flux error covariance is ~~the inverse Hessian, which incorporates the transport,~~  
327 measurement, and background errors at the 4D-Var solution (Eq. 13 in Bowman et al, 2017).

Deleted: analytically

328 Posterior flux uncertainty projected to regions can be estimated analytically based on the methods  
329 described in Fisher and Courtier (1995) and Meirink et al. (2008), using either flux singular vectors  
330 or flux increments obtained during the iterative optimization (e.g., Niwa and Fujii, 2020). In this  
331 study, we rely on a Monte Carlo approach to quantify posterior flux uncertainties following  
332 Chevallier et al. (2010) and Liu et al. (2014), which is simpler and widely used. In this approach,

Deleted: For large-order systems, the posterior errors cannot be explicitly calculated. Consequently,

Deleted: .

333 an ensemble of flux inversions is carried out with an ensemble of priors and simulated observations  
334 to sample the uncertainties of prior fluxes (i.e.,  $\mathbf{B}$  in eq. 1) and observations ( $\mathbf{R}$  in Eq. 1),  
335 respectively. The magnitude of posterior flux uncertainties is a function of assumed uncertainties  
336 in prior fluxes and observations, as well as the density of observations. Since the density of  
337 GOSAT and OCO-2 observations are stable (section 2.3) within their respective data record, we  
338 characterize the posterior flux uncertainties for 2010 and 2015 only, and assume the flux  
339 uncertainties for 2011–2014 are the same as 2010 and flux uncertainties for 2016–2018 are the  
340 same as 2015.

341

## 342 2.5 Evaluation of posterior fluxes

347 Direct NBE estimates from flux towers only provide a spatial representation of roughly 1 – 3  
 348 kilometers (Running et al., 1999), not appropriate to evaluate regional NBE from top-down flux  
 349 inversions. Thus, we use two methods to indirectly evaluate the posterior NBE and its uncertainties.  
 350 One is to compare annual NBE anomalies and seasonal cycle to a gross primary production (GPP)  
 351 product. The other is to compare posterior CO<sub>2</sub> mole fractions to independent (i.e., not assimilated  
 352 in the inversion) aircraft and the NOAA MBL reference observations. The second method has been  
 353 broadly used to indirectly evaluate posterior fluxes from top-down flux inversions (e.g., Stephens  
 354 et al., 2007; Liu and Bowman, 2016; Chevallier et al., 2019; Crowell et al., 2019). In addition to  
 355 these two methods, we also compare the NBE seasonal cycles to three publicly available top-down  
 356 NBE estimates that are constrained by surface CO<sub>2</sub> observations (Tables 3 and 7).

Deleted: of a few

Deleted: observations

Deleted: (i.e., not assimilated in the inversion)

Formatted: Subscript

### 2.5.1 Evaluation against independent gross primary production (GPP) product

358 NBE is a small residual difference between two large terms: total ecosystem respiration (TER)  
 359 and GPP, plus fire. A positive NBE anomaly (i.e., less uptake from the atmosphere) has been  
 360 shown to correspond to reduced GPP caused by climate anomalies (e.g., Bastos et al., 2018), and  
 361 the magnitude of net uptake is proportional to GPP in most biomes observed by flux tower  
 362 observations (e.g., Falk et al., 2008). Since NBE is related not only to GPP, the comparison to GPP  
 363 only serves as a qualitative measure of the NBE quality. For example, we would expect that the  
 364 posterior NBE seasonality to be anti-correlated with GPP in the temperate and high latitudes. In  
 365 this study, we use FLUXSAT GPP (Joiner et al., 2018), which is an upscaled GPP product based  
 366 on flux tower GPP observations and satellite-based geometry adjusted reflectance from the  
 367 MODerate-resolution Imaging Spectroradiometer (MODIS) and solar-induced chlorophyll  
 368 fluorescence observations from Global Ozone Monitoring Experiment – 2 (GOME-2) (Joiner et



372 al., 2013). Joiner et al. (2018) show that the agreement between FLUXSAT-GPP and GPP from  
373 flux towers is better than other available upscaled GPP products.

374 **2.5.2 Evaluation against aircraft and the NOAA marine boundary layer (MBL)**  
375 **reference CO<sub>2</sub> observations**

376 The aircraft observations used in this study include those published in OCO-2 MIP ObsPack  
377 August 2019 (CarbonTracker team, 2019), which include regular vertical profiles from flask  
378 samples collected on light aircraft by NOAA (Sweeney et al., 2015) and other laboratories, regular  
379 (two to four weekly) vertical profiles from the Instituto de Pesquisas Espaciais (INPE) over  
380 tropical South America (SA) (Gatti et al., 2014), and from the Atmospheric Tomography (ATom,  
381 Wofsy et al., 2018), HIAPER Pole-to-Pole (HIPPO, Wofsy et al., 2011), and the O<sub>2</sub>/N<sub>2</sub> Ratio and  
382 CO<sub>2</sub> airborne Southern Ocean Study (ORCAS) (Stephens et al., 2017) aircraft campaigns (Table  
383 3). Figure 2 shows the aircraft observation coverage and density between 2010 and 2018. Most of  
384 the aircraft observations are concentrated over NA. ATom had four (1–4) campaigns between  
385 August 2016 to May 2018, spanning four seasons over the Pacific and Atlantic Ocean. HIPPO had  
386 five (1–5) campaigns over the Pacific, but only HIPPO 3–5 occurred between 2010 and 2011.  
387 HIPPO 1–2 occurred in 2009. Based on the spatial distribution of aircraft observations, we divide  
388 the comparison into nine regions: Alaska, mid-latitude NA, Europe, East Asia, South Asia, Africa,  
389 Australia, Southern Ocean, and South America (Table 4 and Figure 2).

390

391 We calculate several quantities to evaluate the posterior fluxes and their uncertainty with aircraft  
392 observations. One is the monthly mean differences between posterior and aircraft CO<sub>2</sub> mole  
393 fractions. The second is the monthly root mean square errors (RMSE) over each of nine sub-  
394 regions, which is defined as:

Deleted: aircraft campaigns from

Deleted: and

Deleted: regular (two to four weekly) vertical profiles from the Instituto de Pesquisas Espaciais (INPE) over tropical South America (SA) (Gatti et al., 2014),

Deleted: (ORCAS)

Deleted: aircraft campaign

Deleted: and

Deleted: its

$$RMSE = \left( \frac{1}{n} \sum_{i=1}^n (y_{aircraft}^o - y_{aircraft}^b)^2 \right)^{\frac{1}{2}} \quad (2)$$

where  $y_{aircraft}^o$  is the  $i^{th}$  aircraft observation,  $y_{aircraft}^b$  is the corresponding posterior CO<sub>2</sub> mole fraction, sampled at the  $i^{th}$  aircraft location, and  $n$  is the number of aircraft observations over each region. The RMSE is computed over the  $n$  aircraft observations within one of the nine sub-regions.

The mean differences indicate the magnitude of the mean posterior CO<sub>2</sub> bias, while the RMSE includes both random and systematic errors in posterior CO<sub>2</sub>. The bias and RMSE could be due to errors in posterior fluxes, transport, and initial CO<sub>2</sub> concentrations. When errors in transport and initial CO<sub>2</sub> concentrations are smaller than the errors in the posterior fluxes, the magnitude of biases and RMSE indicates the accuracy of the posterior fluxes.

To evaluate the magnitude of posterior flux uncertainty estimates, we compare RMSE against the standard deviation of ensemble simulated aircraft observations (equation 3) from the Monte Carlo method ( $RMSE_{MC}$ ). The quantity  $RMSE_{MC}$  can be written as:

$$RMSE_{MC} = \left[ \frac{1}{nens} \sum_{iens=1}^{nens} ((y_{aircraft}^{b(MC)})_{iens} - y_{aircraft}^{b(MC)})^2 \right]^{\frac{1}{2}} \quad (3)$$

The variable  $(y_{aircraft}^{b(MC)})_{iens}$  is the  $i^{th}$  ensemble member of simulated aircraft observations from Monte Carlo ensemble simulations,  $y_{aircraft}^{b(MC)}$  is the mean, and  $nens$  is the total number of ensemble members. For simplicity, in equation (3), we drop the indices for the aircraft observations used in equation (2). In the absence of errors in transport and initial CO<sub>2</sub> concentrations, when the estimated posterior flux uncertainty reflects the “true” posterior flux uncertainty, we show in the Appendix that:

$$RMSE^2 = R_{aircraft} + RMSE_{MC}^2 \quad (4)$$

Field Code Changed

Deleted: s

Deleted: s

Deleted: either

Deleted: or

Formatted: Subscript

Deleted: or both

Deleted: transport errors

Formatted: Subscript

Deleted: transport errors

where  $R_{aircraft}$  is the aircraft observation error variance, which could be neglected on regional scale,

Deleted: s

We further calculate the ratio  $r$  between  $RMSE$  and  $RMSE_{MC}$ :

$$r = \frac{RMSE}{RMSE_{MC}} \quad (5)$$

A ratio close to one indicates that the posterior flux uncertainty reflects the true uncertainty in the posterior fluxes when the transport errors are small.

The presence of transport errors will make the comparison between  $RMSE$  and  $RMSE_{MC}$  potentially difficult to interpret. Even when  $RMSE_{MC}$  represents the actual uncertainty in posterior fluxes, the  $RMSE$  could be larger than  $RMSE_{MC}$ , since the differences between aircraft observations and model simulated posterior mole fractions  $RMSE$  could be due to errors in both transport and the posterior fluxes, while  $RMSE_{MC}$  only reflects the impact of posterior flux uncertainty on simulated aircraft observations. In this study, we assume the primary sources of  $RMSE$  come from errors in posterior fluxes.

The  $RMSE$  and  $RMSE_{MC}$  comparison only shows differences in  $CO_2$  space. We further calculate the sensitivity of the  $RMSE$  to the posterior flux using the GEOS-Chem adjoint. We first define a cost function  $J$  as:

$$J = RMSE^2 \quad (6)$$

The sensitivity of the mean-square error to a flux,  $x$ , at location  $i$  and month  $j$  is

$$w_{i,j} = \frac{\partial J}{\partial x_{i,j}} \times x_{i,j} \quad (7)$$

Deleted:

456 This sensitivity is normalized by the flux magnitude. Equation 7 can be interpreted as the  
 457 sensitivity of the  $RMSE^2$  to a fractional change in the fluxes. We can estimate the time-integrated  
 458 magnitude of the sensitivity over the entire assimilation window by calculating:

$$459 \quad S_i = \frac{\sum_{j=1}^M |w_{i,j}|}{\sum_{k=1}^P \sum_{j=1}^M |w_{k,j}|} \quad (8)$$

460 where  $P$  is the total number of grid points and  $M$  is the total number of months from the time of  
 461 the aircraft data to the beginning of the inversion. The numerator of equation (8) quantifies the  
 462 absolute total sensitivity of the  $RMSE^2$  to the fluxes at the  $i^{th}$  grid. Normalized by the total absolute  
 463 sensitivity across the globe, the quantity  $S_i$  indicates the relative sensitivity of  $RMSE^2$  to fluxes at  
 464 the  $i^{th}$  grid point. Note that  $S_i$  is unitless, and it only quantifies sensitivity, not the contribution of  
 465 fluxes at each grid to  $RMSE^2$ .

466  
 467 [We use the NOAA MBL reference dataset \(Table 7\) to evaluate the CO<sub>2</sub> seasonal cycle over four](#)  
 468 [latitude bands: 90°N-60°N, 60°N-20°N, 20°N-20°S, and 20°S-90°S. The MBL reference is based](#)  
 469 [on a subset of sites from the NOAA Cooperative Global Air Sampling Network. Only](#)  
 470 [measurements that are representative of a large volume air over a broad region are considered. In](#)  
 471 [the comparison, we first remove the global mean CO<sub>2</sub>](#)  
 472 [\(<https://www.esrl.noaa.gov/gmd/ccgg/trends/global.html>\) from both the NOAA MBL reference](#)  
 473 [and the posterior CO<sub>2</sub>.](#)

## 475 2.6 Regional masks

476 We provide posterior NBE from 2010 – 2018 using [three](#) sets of [regional masks \(Figure 3\)](#), in  
 477 [addition to the](#) gridded product. The regional mask in [Figure 3A](#) is based on a combination of  
 478 seven plant function types condensed from MODIS IGBP and the [TransCom -3 regions](#) (Gurney

Formatted: Subscript

Formatted: Subscript

Formatted: Subscript

Deleted: two

Deleted: aggregated regions

Deleted: , for a few selected FLUXNET tower sites

Deleted: and

Deleted: the underlying

Deleted:

Deleted: A

Deleted: TRANSCOM

Deleted: region mask

et al., 2004), [which is referred as Region Mask 1 \(RM1\) in later description](#). There are 28 regions in Figure 3A: six in NA, four in SA, five in Eurasia (north of 40°N), three in tropical Asia, three in Australia, and seven in Africa. The regional mask in Figure 3B is based on latitude and continents [with 13 regions in total, which is referred as Region Mask 2 \(RM2\) in later description](#). [Figure 3C is the TransCom regional mask with 11 regions on land.](#)

Deleted: , and there are

Deleted: 1.

### 3 Dataset description

We present the [fluxes as globally, latitudinally, and regionally aggregated](#) time series. We show the nine-year average fluxes aggregated into [RM1, RM2, and TransCom](#) regions (Figure 3). The aggregations are geographic (latitude and continent) [and bio-climatic \(biome by continent\)](#). For each region in the geographic and biome aggregations, we show nine-year mean annual net fluxes and uncertainties, and then the annual fluxes for each region as a set of time-series plots. The month-by-month fluxes and uncertainties are available in tabular format, so the actual aggregated fluxes may be readily compared to bottom-up extrapolated fluxes and Earth System models. Users can also aggregate the gridded fluxes and uncertainties based on their own defined regional masks. Table 5 provides a complete list of all data products available in the dataset. In section 4, we describe the major characteristics of the dataset.

Deleted: gridded

Deleted: 28 and 13 geographic

Deleted:

Deleted: ,

Deleted: ), and flux-oriented (for a set of selected flux sites

Deleted:

## 4 Characteristics of the dataset

### 4.1 Global fluxes

The annual atmospheric CO<sub>2</sub> growth rate, which is the sum of fossil fuel emissions and total annual sink over land and ocean, is well-observed by [the](#) NOAA surface CO<sub>2</sub> observing network (<https://www.esrl.noaa.gov/gmd/ccgg/ggrn.php>). We compare the global total flux estimates constrained by GOSAT and OCO-2 with the NOAA CO<sub>2</sub> growth rate from 2010–2018, and discuss the mean

Deleted: (Freidlingstein et al., 2019)

521 carbon sink over land and ocean. Over these nine years, the satellite-constrained atmospheric CO<sub>2</sub>  
522 growth rate agrees with the NOAA observed CO<sub>2</sub> growth rate within the uncertainty of [the](#)  
523 posterior fluxes (Figure 4). The mean annual global surface CO<sub>2</sub> fluxes (in Gt C/yr) [are](#) derived  
524 from the NOAA observed CO<sub>2</sub> growth rate (in ppm/yr) using a conversion factor of 2.124 GtC/ppm  
525 (Le Quéré et al., 2018). The estimated growth rate has the largest discrepancy with the NOAA  
526 observed growth rate in 2014, which may be due to a failure of one of the two solar paddles [of](#)  
527 [GOSAT](#) in May 2014 (Kuze et al., 2016). Over the nine years, the estimated total accumulated  
528 carbon in the atmosphere is  $41.5 \pm 2.4$  GtC, which is slightly lower than the accumulated carbon  
529 based on [the](#) NOAA CO<sub>2</sub> growth rate ( $45.2 \pm 0.4$  GtC). On average, the land sink is  $20 \pm 8\%$  of  
530 fossil fuel emissions, and the ocean sink is  $30 \pm 1\%$  of fossil fuel emissions (Figure 4). These  
531 numbers are within the ranges of the corresponding estimates from GCP 2019 (Freidlingstein et  
532 al., 2019). The mean NBE and ocean sink from GCP 2019 are  $21 \pm 10\%$  ( $\sim 1.0$  GtC estimated  
533 residual NBE uncertainty) and  $26 \pm 5\%$  ( $\sim 0.5$  GtC estimated ocean flux uncertainty) of fossil fuel  
534 emissions respectively between 2010–2018. The GCP NBE here is calculated [as](#) the residual  
535 differences between fossil fuel, ocean fluxes, and atmospheric CO<sub>2</sub> growth rate, and it is also  
536 equivalent to the sum of carbon fluxes from land use changes, land sink, and residual balance  
537 reported by GCP. Over these nine years, we estimate that the land sink ranges from 37% of fossil  
538 fuel emissions in 2011 (a La Niña year) to only 5% in 2015 (an El Niño year), consistent with [the](#)  
539 [range estimated by](#) GCP [of](#) 35% in 2011 to 7% in 2015. We estimate that the ocean sinks range  
540 from 39% in 2015 to 23% of fossil fuel emissions in 2012, larger than the GCP estimated ocean  
541 flux ranges of 25% to 28% of fossil fuel emissions (Freidlingstein et al., 2019).

#### 542 4.2 Mean regional fluxes and uncertainties

Deleted: is

Deleted: estimated range



Figure 5 shows the nine-year mean regional annual fluxes, uncertainty, and its variability between 2010–2018. Table 6 shows an example of the dataset corresponding to Figure 5 A, [D](#), and [G](#). It shows [that](#) large net carbon uptake occurs over Eurasia, NA, and [the](#) Southern Hemisphere (SH) mid-latitudes. The largest net carbon uptake is over [the](#) eastern US ( $-0.4 \pm 0.1$  GtC ( $1\sigma$  uncertainty)) and high latitude Eurasia ( $-0.5 \pm 0.1$  GtC) (Figure 5A, B). We estimate a net land carbon sink of  $2.5 \pm 0.3$  GtC/year between 2010–2013 over the NH mid to high latitudes, which agrees with  $2.4 \pm 0.6$  GtC estimates over the same time periods based on a two-box model (Ciais et al., 2019). Net uptake in the tropics ranges from close-to-neutral in tropical South America ( $0.1 \pm 0.1$  GtC) to a net source in northern Africa ( $0.6 \pm 0.2$  GtC) (Figure 5A, B). The tropics exhibit both large uncertainty and large variability. The NBE interannual variability over northern Africa and tropical SA are 0.5 GtC and 0.3 GtC respectively, larger than the 0.2 GtC and 0.1 GtC uncertainty (Figure [5D, E](#)). We also find collocation of regions with large NBE and GPP interannual variability (Figure S4). [The availability of flux estimates over the broadly used TransCom regions make it easy to compare to previous studies. For example, we estimate that the annual net carbon uptake over North America is  \$0.7 \pm 0.1\$  GtC/year with 0.2 GtC variability between 2010 and 2018, which agrees with  \$0.7 \pm 0.5\$  GtC/year estimates based on surface CO<sub>2</sub> observations between 1996-2007 \(Peylin et al., 2013\).](#)

### 4.3 Interannual variabilities and uncertainties

Here we present hemispheric and regional NBE interannual variabilities and corresponding uncertainties (Figures 6 and 7, and corresponding tabular data files). In Figure 6, we further divide the globe into three large latitude bands: tropics (20°S–20°N), NH extra-tropics (20°N–85°N), and SH extra-tropics (60°S–20°S). The tropical NBE contributes 90% to the global NBE interannual

Deleted: C

Deleted: E

Deleted: 4

Deleted: 0

Deleted: 5C

Deleted: D

Formatted: Subscript

574 variability (IAV). The IAV of NBE over the extra-tropics is only about one-third of that over the  
575 tropics. The dominant role of tropical NBE in the global IAV of NBE agrees with Figure 4 in  
576 Sellers et al. (2018). The top-down global annual NBE anomaly is within the 1.0 GtC/yr  
577 uncertainty of residual NBE (i.e., fossil fuel – atmospheric growth – ocean sink) calculated from  
578 GCP-2019 (Friedlinton et al., 2019) (Figure 6).

579

580 Figure 7 shows the annual NBE anomalies and uncertainties over a few selected regions [based on](#)  
581 [RM1](#). Positive NBE indicates reduced net uptake relative to the 2010–2018 mean, and vice versa.  
582 Also shown in Figure 7 are GPP anomalies estimated from FLUXSAT. Positive GPP indicates  
583 increased productivity, and vice versa. GPP drives NBE in years where anomalies are inversely  
584 correlated (e.g., positive NBE and negative GPP), and TER drives NBE in years where anomalies  
585 of GPP and NBE have the same sign or [are](#) weakly correlated. Over tropical SA evergreen  
586 broadleaf forest, the largest positive NBE anomalies occur during [the](#) 2015–2016 El Niño,  
587 corresponding to large reductions in productivity, consistent with Liu et al. (2017). In 2017, the  
588 region sees increased net uptake and increased productivity, implying a recovery from the 2015–  
589 2016 El Niño event. The variability in GPP explains 80% of NBE variability over this region over  
590 the nine-year period. In Australian shrubland, our inversion captures the increased net uptake in  
591 2010 and 2011 due to increased precipitation (Poulter et al., 2014) and increased productivity. The  
592 variability in GPP explains 70% of the interannual variability in NBE. Over tropical south America  
593 [savanna](#), the NBE interannual variability also shows strong negative correlations with GPP, with  
594 GPP explaining 40% of NBE interannual variability. Over the mid-latitude regions where the IAV  
595 is small, the  $R^2$  between GPP and NBE is also small (0.0–0.5) as expected. But the increased net  
596 uptake generally corresponds to increased productivity. We also do not expect perfect negative

Deleted: Savanna

598 correlation between NBE anomalies and GPP anomalies, as discussed in section 2.5. The  
599 comparison between NBE and GPP provides insight into when and where net fluxes are likely  
600 dominated by productivity.

601

#### 602 4.4 Seasonal cycle

603 We provide the regional mean NBE seasonal cycle, its variability, and uncertainty based on the  
604 three regional masks (Table 5). Here we briefly describe the characteristics of the NBE seasonal  
605 cycle over the 11 TransCom regions, and its comparison to three independent top-down inversion  
606 results based on surface CO<sub>2</sub>, which are CT-Europe (e.g., van der Laan-Luijkx et al., 2017) CAMS  
607 (Chevallier et al., 2005), and Jena CarbonScope (Rödenbeck et al., 2003). CMS-Flux-NBE differs the  
608 most from surface-CO<sub>2</sub> based inversions over the South American Tropical, Northern Africa,  
609 tropical Asia, and NH boreal regions. The CMS-Flux NBE has a larger seasonal cycle amplitude  
610 over tropical Asia and Northern Africa, where the surface CO<sub>2</sub> constraint is weak, while it has a  
611 smaller seasonal cycle amplitude over the boreal region; this may be due to the sparse satellite  
612 observations over the high latitudes and weaker seasonal amplitude of the prior CARDAMOM  
613 fluxes. The comparison to FluxSat GPP can only qualitatively evaluate the NBE seasonal cycle,  
614 but cannot differentiate among different estimates. In general, the months that have larger  
615 productivity corresponds to months with a net uptake of carbon from the atmosphere, especially  
616 over the NH (Figure 8). More research is still needed to understand the seasonal cycles of NBE,  
617 including its phase (i.e., transition from source to sink) and amplitude (peak-to-trough difference),  
618 and its relationships with GPP and respiration.

619

#### 620 5 Evaluation against independent aircraft CO<sub>2</sub> observations

Deleted: a top-down CO<sub>2</sub> constrained

Deleted: and

Deleted: and

Moved down [3]: The seasonal cycle of NBE, including its phase (i.e., transition from source to sink) and amplitude (peak-to-trough difference), have large uncertainties, not only over the less-observed tropical regions, but also over the extra-tropics (e.g., Yang et al., 2007; Keppel-Aleks et al., 2012).

Formatted: Subscript

Deleted: Figure 8 shows NBE and GPP seasonal cycles for six selected regions.

Formatted: Subscript

Formatted: Subscript

Deleted: .

Deleted: The NH mid-to-high latitudes have larger seasonal cycle amplitudes (Figure 8A, B) compared to the other regions, and their NBE seasonalities are more closely linked to that of GPP ( $R^2 = 0.9$ ). In the tropics, the relationship between NBE and GPP seasonality is less clear partially due to the weak seasonality of NBE (Figure 8E, F). The variability and uncertainty of monthly mean fluxes are larger over the tropics and the SH extratropics than over the NH extratropics. The

Moved (insertion) [3]

Deleted: , have large uncertainties, not only over the less-observed tropical regions, but also over the extra-tropics (e.g., Yang et al., 2007; Keppel-Aleks et al., 2012)

## 645 5.1 Comparison to aircraft observations over nine sub-regions

646 In this section, we evaluate posterior CO<sub>2</sub> against aircraft observations over [the](#) nine sub-regions  
647 listed in Table 4 and Figure 2. We compare the posterior [CO<sub>2</sub>](#) to aircraft CO<sub>2</sub> mole fractions above  
648 [the](#) planetary boundary layer and up to mid troposphere (1–5 km) at the locations and time of  
649 aircraft observations, and then calculate the monthly mean error statistics between 1–5 km. The  
650 aircraft observations between 1–5 km are more sensitive to regional fluxes (Liu et al., 2015; Liu  
651 and Bowman, 2016). Scatter plots in the left column of Figure 9 show regional monthly mean de-  
652 trended aircraft CO<sub>2</sub> observations (x-axis) versus the simulated detrended posterior CO<sub>2</sub> (y-axis).  
653 We used [the](#) NOAA global CO<sub>2</sub> trend to detrend both the observations and model simulated mole  
654 fractions ([ftp://aftp.cmdl.noaa.gov/products/trends/co2/co2\\_trend\\_gl.txt](ftp://aftp.cmdl.noaa.gov/products/trends/co2/co2_trend_gl.txt)). Over the NH regions (A,  
655 B, C, D) and Africa (F), the R<sup>2</sup> is [greater than or equal to](#) 0.9, which indicates that the posterior  
656 CO<sub>2</sub> captures the observed seasonality. The low R<sup>2</sup> (0.7) value in South Asia is caused by one  
657 outlier. Over [the](#) Southern Ocean, Australia, and SA, the R<sup>2</sup> is between 0.2 and 0.4, reflecting  
658 weaker CO<sub>2</sub> seasonality over these regions [and possible bias in ocean flux estimates \(see](#)  
659 [discussions later](#)).  
660

661 The right panel of Figure 9 shows the monthly mean differences between posterior CO<sub>2</sub> and aircraft  
662 observations (black),  $RMSE$  (equation 2) (blue line), and  $RMSE_{MC}$  (equation 3) (red line). The  
663 magnitude of [the](#) mean differences between [the](#) posterior CO<sub>2</sub> and aircraft observations is less than  
664 0.5 ppm except over [the](#) Southern Ocean, which has a -0.8 ppm bias. The mean differences between  
665 posterior CO<sub>2</sub> and aircraft observations are primarily caused by errors in transport and biases in  
666 assimilated satellite observations, while  $RMSE_{MC}$  is ‘internal flux error’ projected into mole  
667 fraction space. [With the exception of the Southern Ocean, for all regions mean bias is significantly](#)

Formatted: Subscript

Deleted: or above

Deleted: the number of aircraft observations (blue bar, right y-axis),

Deleted:

672 less than  $RMSE_{MC}$ , which suggests that transport and data bias in satellite observations may be  
673 much smaller than the internal flux errors. [Note that  \$RMSE\_{MC}\$  is smaller than  \$RMSE\$  over the first](#)  
674 [~six months of simulation, which may indicate a dominant impact of errors in transport and initial](#)  
675 [CO<sub>2</sub> concentration on posterior CO<sub>2</sub>  \$RMSE\$ .](#)

676 ▾ Deleted: ¶  
677 As demonstrated in section 2.5, comparing  $RMSE$  and  $RMSE_{MC}$  is a test of the accuracy of posterior  
678 flux uncertainty estimate. Over all the regions, the differences between  $RMSE$  and  $RMSE_{MC}$  are  
679 smaller than 0.3 ppm, which indicates a comparable magnitude between empirical posterior flux  
680 uncertainty estimates from [the](#) Monte Carlo method and the actual posterior flux uncertainty over  
681 the regions that these aircraft observations are sensitive to. These aircraft observations are sensitive  
682 to fluxes over a broad region as shown in Figure S5.

## 684 5.2 Comparison to aircraft observations from ATom and HIPPO aircraft campaigns

685 Figures 10 and 11 show comparisons to aircraft CO<sub>2</sub> from ATom 1–4 campaigns spanning four  
686 seasons, and HIPPO 3–5 over the Pacific Ocean between 1–5 km. The vertical curtain comparisons  
687 are shown in Figure S6 and S7. The mean differences between posterior CO<sub>2</sub> and aircraft CO<sub>2</sub> are  
688 quite uniform (within 0.5 ppm) throughout the column except over the Atlantic Ocean during  
689 ATom 1–2 and the Southern Ocean during ATom 1 (Figures S6 and S7). Also shown in Figures  
690 10 and 11 are  $RMSE$  of each aircraft campaign (middle column) and the ratio between  $RMSE$  and  
691  $RMSE_{MC}$  (right column). A ratio larger than one between  $RMSE$  and  $RMSE_{MC}$  indicates errors in  
692 either transport or [underestimation of the](#) posterior flux uncertainty (section 2.5).

Deleted: low

Deleted: estimates

697 Over most of [the](#) flight tracks during ATom 1–4, the posterior CO<sub>2</sub> errors are between -0.5 and 0.5  
 698 ppm, the *RMSE* is smaller than 0.5 ppm, and the ratio between *RMSE* and *RMSE<sub>MC</sub>* is smaller than  
 699 or equal to 1. However, off the coast of Africa during ATOM -1 and -2 and over [the](#) Southern  
 700 Ocean during ATOM-1, the mean differences between posterior CO<sub>2</sub> and aircraft observations are  
 701 larger than 0.5 ppm. During ATOM-1 (29 July – 23 Aug 2016), the mean differences between  
 702 posterior CO<sub>2</sub> and aircraft CO<sub>2</sub> show large negative biases, while during ATOM-2 (26 Jan 2017–  
 703 21 Feb 2017), it has large positive biases off the coast of Africa. The ratio between *RMSE* and  
 704 *RMSE<sub>MC</sub>* is significantly larger than one over these regions, which indicates an underestimation of  
 705 posterior flux uncertainty or large magnitude of transport errors during that time period.

706

707 We further run adjoint sensitivity analyses over the three regions with ratios significantly larger  
 708 than one to identify the posterior fluxes that could contribute to the large differences between  
 709 posterior CO<sub>2</sub> and aircraft observations during ATOM 1–2. We run the adjoint model backward  
 710 for three months from the observation time and calculate  $S_i$  [as](#) defined in equation (7). [The adjoint](#)  
 711 sensitivity analysis indicates that the large mismatch between aircraft observations and model  
 712 simulations during ATOM-1 and -2 off the coast of Africa could be potentially driven by errors in  
 713 posterior fluxes over tropical Africa (Figure S8). [The large posterior CO<sub>2</sub> errors and large ratio](#)  
 714 [between \*RMSE\* and \*RMSE<sub>MC</sub>\* over \[the\]\(#\) Southern Ocean during ATOM-1 are driven by flux errors](#)  
 715 in oceanic fluxes around 30°S and over Australia (Figure S9), [which also contribute to the large](#)  
 716 [errors in comparison to aircraft observations over the Southern Ocean shown in Figure 9 H.](#)

717

718 During the HIPPO aircraft campaigns, the absolute errors in posterior CO<sub>2</sub> across [the](#) Pacific are  
 719 less than 0.5 ppm except over the Arctic Ocean and over Alaska in summer (Figure 11), consistent

Deleted: A

Deleted: These

Deleted:

Deleted: .

724 with Figure 10A. The large errors over the Arctic Ocean may be related to both transport errors  
725 and the accuracy of high latitude fluxes. Byrne et al. (2020) provide a brief summary of [the](#)  
726 challenges in simulating CO<sub>2</sub> over high latitudes [using a transport model](#) with 4° x 5° resolution.  
727 Increasing the resolution of the transport model may reduce transport errors over high latitudes.

Deleted: these

Deleted: transport model

728  
729 We run adjoint sensitivity analysis over the high-latitude regions where the differences between  
730 posterior CO<sub>2</sub> and aircraft observations are large (Figure 11). The adjoint sensitivity analysis  
731 (Figure S10) shows that the large errors over these regions could be driven by errors in fluxes over  
732 Alaska as well as broad NH mid-latitude regions.

### 734 [5.3 Comparison to MBL reference sites](#)

Formatted: Font: Bold

735 [Since MBL reference sites sample air over broad regions, the comparison to detrended MBL](#)  
736 [observations indirectly evaluates the NBE over large regions. Figure 12 shows the comparison](#)  
737 [over four latitude bands. The uncertainty of posterior CO<sub>2</sub> concentration is from the MC method.](#)  
738 [Except over 90°S-20°S, the differences between observations and posterior CO<sub>2</sub> are within](#)  
739 [posterior CO<sub>2</sub> uncertainty estimates. Over 90°S-20°S, the posterior CO<sub>2</sub> has positive bias in 2013](#)  
740 [and 2014 and negative bias and much weaker seasonality between Jan 2015 – Dec 2018 compared](#)  
741 [to observations, which indicates possible biases in Southern Ocean flux estimates. The low bias](#)  
742 [over Southern Ocean is consistent with aircraft comparison during OCO-2 period \(Figures 9 and](#)  
743 [10\). The posterior CO<sub>2</sub> have smallest bias and random errors over the tropical latitude band. The](#)  
744 [R<sup>2</sup> is above 0.9 over NH mid to high latitudes, consistent with Figure 9.](#)

Formatted: Subscript

Formatted: Subscript

Formatted: Subscript

## 745 6 Discussion

749 Evaluation of posterior flux uncertainty estimates by comparing posterior CO<sub>2</sub> error statistics  
 750 (*RMSE*, Equation 2) with the standard deviation of ensemble simulated CO<sub>2</sub> from Monte Carlo  
 751 uncertainty quantification method (*RMSE<sub>MC</sub>*, equation 3) has its limitations. A comparable *RMSE*  
 752 and *RMSE<sub>MC</sub>* indicates a small magnitude of transport errors and reasonable posterior uncertainty  
 753 estimates. A much larger *RMSE* than *RMSE<sub>MC</sub>* could be due to errors in either transport or  
 754 underestimation of the posterior flux uncertainty or both. The presence of transport errors makes  
 755 the interpretation of the *RMSE* and *RMSE<sub>MC</sub>* complex. A better, independent quantification of  
 756 transport errors is needed in the future in order to rigorously use the comparison statistics between  
 757 aircraft observations and posterior CO<sub>2</sub> to diagnose flux errors.

758

759 Comparison to aircraft observations shows regionally-dependent accuracy in posterior fluxes.  
 760 ATom observations show seasonally-dependent biases over the Atlantic, implying possible  
 761 seasonally dependent errors in posterior fluxes over northern to central Africa. Therefore, we  
 762 recommend combining NBE with other ancillary variables, e.g., GPP, to better understand carbon  
 763 dynamics. Combining NBE with component carbon fluxes can shed light on the processes  
 764 controlling the changes of NBE (e.g., Bowman et al, 2017; Liu et al., 2017). NBE can be written  
 765 as:

$$766 \text{ NBE} = \text{TER} + \text{fire} - \text{GPP} \quad (8)$$

767 where TER is total ecosystem respiration (TER) (Figure 1). Satellite carbon monoxide (CO)  
 768 observations provide constraints on fire emissions (Arellano et al, 2006, van der Werf, 2008; Jones  
 769 et al, 2009; Jiang et al., 2015, Bowman et al, 2017; Liu et al., 2017). In addition to the FLUXSAT-  
 770 GPP product used here, solar induced chlorophyll fluorescence (SIF) can be directly used as a

Deleted: When

Deleted: are similar in magnitude, this

Deleted: to



774 proxy for GPP (e.g., Parazoo et al, 2014). Once NBE, fire, and GPP carbon fluxes are quantified,  
775 TER can be calculated as a residual (e.g., Bowman et al, 2017; Liu et al., 2017, 2018).

776

777 Because of the diffusive manner of atmospheric transport and the limited observation coverage,  
778 the gridded flux values are not independent from each other. The errors and uncertainties of the  
779 fluxes at each individual grid point are larger than regional aggregated fluxes. [Interpreting NBE at](#)  
780 [each individual grid point requires caution. But at the same time, satellite CO<sub>2</sub> constrained NBE](#)  
781 [can potentially resolve fluxes at spatial scales smaller than the traditional TransCom regions. Here,](#)  
782 [we provide regional fluxes at two predefined regions in addition to TransCom. We encourage data](#)  
783 [users to use the data at appropriate regional scales.](#)

784

785 The variability and changes are more robust than the mean NBE fluxes from top-down flux  
786 inversions in general (Baker et al., 2006b). The errors in transport and potential biases in  
787 observations are mostly stable in time, so biases in the mean fluxes tend to cancel out when  
788 computing interannual variability and year-to-year changes (Schuh et al., 2019; Crowell et al.,  
789 2019).

790

791 The global fossil fuel emissions have ~5% uncertainty (GCP, 2019). However, they are regionally  
792 inhomogeneous. We neglect the uncertainties in fossil fuel emissions, which will introduce  
793 additional error in regions of rapid fossil fuel growth or in areas with noisier statistics (Yin et al.,  
794 2019). In the future, we will account for uncertainties in fossil fuel emissions.

795

Deleted: relative

Deleted: For the same reason, comparing

Deleted: with flux tower observations needs

Deleted: , though we provide NBE at a few flux tower sites

Formatted: Subscript

Deleted: ¶

801 The posterior NBE includes all types of land fluxes except fossil fuel emissions, which is  
802 equivalent to the sum of land use change fluxes and land sinks published by [the](#) GCP. The sum of  
803 regional NBE and fossil fuel emissions is an index of the contribution of any specific region to the  
804 changes of [the](#) atmospheric CO<sub>2</sub> growth rate. Even over the continental US, where fossil fuel  
805 emissions are ~1.5 GtC/year, the changes of regional NBE can significantly modify contributions  
806 to the changes of atmospheric CO<sub>2</sub> (Liu et al., 2018). Since NBE has high variability and its  
807 predicted changes in the future are likely to have large uncertainties, quantifying regional NBE is  
808 critical to monitoring regional contributions to atmospheric CO<sub>2</sub> growth rate, and ultimately to  
809 guide mitigation to limit warming to 1.5°C above pre-industrial levels ([IPCC, AR6](#)).

810

## 811 7 Summary

812 Terrestrial biosphere carbon fluxes are the largest contributor to the interannual variability of the  
813 atmospheric CO<sub>2</sub> growth rate. Therefore, monitoring its change at regional scales is essential for  
814 understanding how it responds to CO<sub>2</sub>, climate and land use. Here, we present the longest terrestrial  
815 flux estimates and their uncertainties constrained by X<sub>CO2</sub> from 2010–2018 on self-consistent  
816 global and regional scales (CMS-Flux NBE 2020). We qualitatively evaluate the net flux estimates  
817 by comparing its variability with GPP variability, and provide comprehensive evaluation of  
818 posterior fluxes and the uncertainties by comparing posterior CO<sub>2</sub> with independent [CO<sub>2</sub>](#)  
819 [observations from](#) aircraft [and the NOAA MBL reference sites](#). The estimated posterior flux  
820 uncertainty agrees with the expected uncertainty in the posterior fluxes based on the comparison  
821 to aircraft CO<sub>2</sub> observations. This dataset can be used in understanding controls on regional NBE  
822 interannual variability, evaluating biogeochemical models, and [supporting the monitoring of](#)  
823 regional contributions to [changes in atmospheric CO<sub>2</sub>](#).

Deleted: CO<sub>2</sub>

Deleted: provide support

Deleted: the

Deleted: of the

Deleted: the

829

## 830 8 Data availability and future update

831 The CMS-Flux NBE 2020 data [are](#) available at: <https://doi.org/10.25966/4v02-c391> (Liu et al.,  
832 2020). The regional aggregated fluxes are provided as *csv* files with file size ~10MB, and the  
833 gridded data is provided in NetCDF format with file size ~[1.4 GB](#). The full ensemble [of](#) posterior  
834 fluxes used to estimate posterior flux uncertainties are provided in NetCDF format with file size  
835 ~[30MB](#). Table 7 lists the sources of the data used in producing and evaluating the CMS-Flux NBE  
836 2020 data product.

837

838 The quality of  $X_{CO_2}$  from satellite observations is continually improving. The OCO-2 v10  $X_{CO_2}$   
839 [has been](#) released in June 2020, [along with](#) the full GOSAT record (June 2009–Jan 2020) processed  
840 [by](#) the same retrieval algorithm as OCO-2. Continuing to improving the quality of satellite  
841 observations and extending the NBE estimates beyond 2018 in the future will help us better  
842 understand interactions between terrestrial biosphere carbon cycle and climate and provide support  
843 in monitoring the regional contributions to the changes of atmospheric  $CO_2$ . Thus, we plan a future  
844 update of the dataset on an annual basis, with a goal to support current scientific research and  
845 policy making.

## 846 9 Author contributions

847 JL designed the study and led the writing of the paper in close collaboration with KB and DS. LB  
848 helped generate the plots and created all the data files. AAB provided the prior of the terrestrial  
849 biosphere carbon fluxes. NP helped interpret the GPP evaluation. DM and DC generated the prior  
850 ocean carbon fluxes. TO generated the ODIAC fossil fuel emissions. JJ provided the FLUXSAT  
851 GPP product. BD and SW provided and contributed to the interpretation of HIPPO aircraft  $CO_2$

Deleted: is

Deleted: 10MB

Deleted: 20MB

Deleted: will be

Deleted:

Deleted: , and

Deleted: by

Deleted: will be released around the same time

860 observation comparisons. BS, KM, and CS provided ORCAS aircraft CO<sub>2</sub> observations and  
861 contributed interpretation of aircraft CO<sub>2</sub> observation comparisons. LVG and JM provided INPE  
862 aircraft CO<sub>2</sub> observations and contributed interpretation of aircraft CO<sub>2</sub> observation comparisons.  
863 CS and KM provided ATom and [the](#) NOAA aircraft CO<sub>2</sub> observations and contributed  
864 interpretation of aircraft CO<sub>2</sub> observation comparisons. We furthermore acknowledge funding  
865 from the EU for the ERC project “ASICA” (grant number 649087) to Wouter Peters (Groningen  
866 University) and EU and NERC (UK) funding to Emanuel Gloor (University of Leeds), which  
867 contributed to the INPE Amazon greenhouse sampling program. All authors contributed to the  
868 writing, and have reviewed and approved the paper.

## 869 10 Competing interest

870 The authors declare that they have no conflict of interest.

## 871 Acknowledgement

872 Resources supporting this work were provided by the NASA High-End Computing (HEC)  
873 Program through the NASA Advanced Supercomputing (NAS) division at Ames Research Center.  
874 We acknowledge the funding support from NASA OCO-2/3 Science Team, Carbon Monitoring  
875 System (CMS), and Making Earth Science Data Records for Use in Research Environments  
876 (MEaSUREs) programs. Tomohiro Oda is supported by the NASA Carbon Cycle Science program  
877 (grant no. NNX14AM76G). We acknowledge EU and NERC (UK) funding to Emanuel Gloor,  
878 University of Leeds which substantially contributed to the INPE Amazon greenhouse sampling  
879 program. [CarbonTracker Europe results provided by Wageningen University in collaboration with](#)  
880 [the ObsPack partners \(http://www.carbontracker.eu\)](#). Part of the research was carried out at Jet  
881 Propulsion Laboratory, Caltech.

Formatted: Font: 12 pt

Formatted: Font: (Default) Times New Roman

Formatted: Hyperlink, Font: (Default) Times New Roman,  
Font color: Auto

Formatted: Font: (Default) Times New Roman

Field Code Changed

## 883 Appendix

884 As shown in Kalnay (2003):

885  $RMSE^2 = R_{aircraft} + HP^aH^T$  (A.1)

886 where  $R_{aircraft}$  is the aircraft observation error variance, and  $P^a$  is the posterior flux error  
887 covariance. The  $H$  is linearized observation operator, which transfers posterior flux errors to  
888 aircraft observation space, and  $H^T$  is its adjoint. In the Monte Carlo method, the posterior flux  
889 error covariance  $P^a$  is approximated by:

890  $P^a = \frac{1}{nens} X^a X^{aT}$  (A.2)

891 where  $X^a$  is the ensemble perturbations written as:

892  $X^a = x^a - \bar{x}^a$  (A.3)

893 where  $\bar{x}^a$  is the ensemble posterior fluxes from Monte Carlo, and  $\bar{x}^a$  is the mean.

894 Therefore,  $HP^aH^T$  can be written as:

895  $HP^aH^T = \frac{1}{nens} [h(x^a) - h(\bar{x}^a)][h(x^a) - h(\bar{x}^a)]^T$  (A.4)

896 The right hand side is the same as the definition of  $RMSE_{MC}$  in the main text.

897 Therefore, when the posterior flux uncertainty estimated by Monte Carlo method represents the  
898 actual uncertainty in posterior fluxes, equation (A.1) can be written as:

899  $RMSE^2 = R_{aircraft} + RMSE_{MC}^2$  (A.5).

900 It is the same as equation (3) in the main text.

## 901 References

902 Arellano Jr, A.F., Kasibhatla, P.S., Giglio, L., Van der Werf, G.R., Randerson, J.T., and Collatz,  
903 G.J.: Time-dependent inversion estimates of global biomass-burning CO emissions using  
904 Measurement of Pollution in the Troposphere (MOPITT) measurements, J. Geophys. Res:  
905 Atmos., 111, D09303, <https://doi.org/10.1029/2005JD006613>, 2006.  
906

Deleted:

Deleted: i

Baker, D.F., Doney, S.C., and Schimel, D.S.: Variational data assimilation for atmospheric CO<sub>2</sub>, *Tellus B: Chem. Phys. Meteorol.*, 58, 359-365, <https://doi.org/10.1111/j.1600-0889.2006.00218.x>, 2006a.

Baker, D.F., Law, R.M., Gurney, K.R., Rayner, P., Peylin, P., Denning, A.S., Bousquet, P., Bruhwiler, L., Chen, Y.H., Ciais, P., and Fung, I.Y.: TransCom 3 inversion intercomparison: Impact of transport model errors on the interannual variability of regional CO<sub>2</sub> fluxes, 1988–2003, *Global Biogeochem. Cy.*, 20, GB1002, <https://doi.org/10.1029/2004GB002439>, 2006b.

Bastos, A., Friedlingstein, P., Sitch, S., Chen, C., Mialon, A., Wigneron, J.-P., Arora, V. K., Briggs, P. R., Canadell, J. G., and Ciais, P.: Impact of the 2015/2016 El Niño on the terrestrial carbon cycle constrained by bottom-up and top-down approaches. *Philos. Trans. R Soc. Lond. B. Biol. Sci.*, 373, 1760, <https://doi.org/10.1098/rstb.2017.0304>, 2018.

Bloom, A.A., Exbrayat, J.F., van der Velde, I.R., Feng, L., and Williams, M.: The decadal state of the terrestrial carbon cycle: Global retrievals of terrestrial carbon allocation, pools, and residence times. *Proc. Natl Acad. Sci.*, 113, 1285-1290, 2016.

Bloom, A. A., Bowman, K. W., Liu, J., Konings, A. G., Worden, J. R., Parazoo, N. C., Meyer, V., Reager, J. T., Worden, H. M., Jiang, Z., Quetin, G. R., Smallman, T. L., Exbrayat, J.-F., Yin, Y., Saatchi, S. S., Williams, M., and Schimel, D. S.: Lagged effects dominate the inter-annual variability of the 2010–2015 tropical carbon balance, *Biogeosciences Discuss.*, <https://doi.org/10.5194/bg-2019-459>, in review, 2020.

Bowman, K.W., Liu, J., Bloom, A.A., Parazoo, N.C., Lee, M., Jiang, Z., Menemenlis, D., Gierach, M.M., Collatz, G.J., Gurney, K.R., and Wunch, D.: Global and Brazilian carbon response to El Niño Modoki 2011–2010, *Earth Space Sci.*, 4, 637-660, <https://doi.org/10.1002/2016EA000204>, 2017.

Brix, H., Menemenlis, D., Hill, C., Dutkiewicz, S., Jahn, O., Wang, D., Bowman, K., and Zhang, H.: Using Green's Functions to initialize and adjust a global, eddying ocean biogeochemistry general circulation model, *Ocean Model.*, 95, 1-14, <https://doi.org/10.1016/j.ocemod.2015.07.008>, 2015.

Byrd, R.H., Nocedal, J., and Schnabel, R.B.: Representations of quasi-Newton matrices and their use in limited memory methods, *Math. Program.*, 63, 129-156, <https://doi.org/10.1007/BF01582063>, 1994.

Byrne, B., Liu, J., et al.: Improved constraints on northern extratropical CO<sub>2</sub> fluxes obtained by combining surface-based and space-based atmospheric CO<sub>2</sub> measurements, *JGR-Atmosphere*, (minor revision), 2020

Carroll, D., Menemenlis, D., Adkins, J. F., Bowman, K. W., Brix, H., Dutkiewicz, S., et al.: The ECCO-Darwin Data-assimilative Global Ocean Biogeochemistry Model: Estimates of Seasonal to Multi-decadal Surface Ocean pCO<sub>2</sub> and Air-sea CO<sub>2</sub> Flux. *Journal of Advances in Modeling Earth Systems*, 12, e2019MS001888. <https://doi.org/10.1029/2019MS001888>, 2020

Formatted: Justified

Deleted: Carroll, D., Menemenlis, D., Adkins, J.:

Deleted: The ECCO-Darwin Data-assimilative Global Ocean Biogeochemistry Model: Estimates of Seasonal to Multi-decadal Surface Ocean pCO<sub>2</sub> and Air-sea CO<sub>2</sub> Flux. *Journal of Advances in Modeling Earth Systems* (minor revision), 2020

Carbontracker Team; (2019) : Compilation of near real time atmospheric carbon dioxide data: obspack\_co2\_1\_NRT\_v5.0 2019-08-13; NOAA Earth System Research Laboratory, Global Monitoring Division. <http://doi.org/10.25925/20190813>

Chevallier, F., Fisher, M., Peylin, P., Serrar, S., Bousquet, P., Bréon, F.M., Chédin, A., and Ciais, P.: Inferring CO<sub>2</sub> sources and sinks from satellite observations: Method and application to TOVS data, *J. Geophys. Res.-Atmos.*, 110, D24309, <https://doi.org/10.1029/2005JD006390>, 2005.

Chevallier, F., Ciais, P., Conway, T.J., Aalto, T., Anderson, B.E., Bousquet, P., Brunke, E.G., Ciattaglia, L., Esaki, Y., Fröhlich, M., and Gomez, A.: CO<sub>2</sub> surface fluxes at grid point scale estimated from a global 21 year reanalysis of atmospheric measurements, *J. Geophys. Res.*, 115, D21307, <https://doi.org/10.1029/2010JD013887>, 2010.

Chevallier, F., Remaud, M., O'Dell, C. W., Baker, D., Peylin, P., and Cozic, A.: Objective evaluation of surface- and satellite-driven carbon dioxide atmospheric inversions, *Atmos. Chem. Phys.*, 19, 14233–14251, <https://doi.org/10.5194/acp-19-14233-2019>, 2019.

Ciais, P., Tan, J., Wang, X., Roedenbeck, C., Chevallier, F., Piao, S.L., Moriarty, R., Broquet, G., Le Quééré, C., Canadell, J.G., and Peng, S.: Five decades of northern land carbon uptake revealed by the interhemispheric CO<sub>2</sub> gradient, *Nature*, 568, 221–225, <https://doi.org/10.1038/s41586-019-1078-6>, 2019.

Conway, T. J., Tans, P. P., Waterman, L. S., Thoning, K. W., Kitzis, D. R., Masarie, K. A., and Zhang, N. (1994). Evidence for interannual variability of the carbon cycle from the National Oceanic and Atmospheric Administration/Climate Monitoring and Diagnostics Laboratory Global Air Sampling Network, *J. Geophys. Res.*, 99 (D11), 22831–22855, doi:10.1029/94JD01951.

Crisp, D., Fisher, B. M., O'Dell, C., Frankenberg, C., Basilio, R., Bösch, H., Brown, L. R., Castano, R., Connor, B., Deutscher, N. M., Eldering, A., Griffith, D., Gunson, M., Kuze, A., Mandrake, L., McDuffie, J., Messerschmidt, J., Miller, C. E., Morino, I., Natraj, V., Notholt, J., O'Brien, D. M., Oyafuso, F., Polonsky, I., Robinson, J., Salawitch, R., Sherlock, V., Smyth, M., Suto, H., Taylor, T. E., Thompson, D. R., Wennberg, P. O., Wunch, D., and Yung, Y. L.: The ACOS CO<sub>2</sub> retrieval algorithm – Part II: Global X<sub>CO2</sub> data characterization, *Atmos. Meas. Tech.*, 5, 687–707, <https://doi.org/10.5194/amt-5-687-2012>, 2012.

Crisp, D., Pollock, H. R., Rosenberg, R., Chapsky, L., Lee, R. A. M., Oyafuso, F. A., Frankenberg, C., O'Dell, C. W., Bruegge, C. J., Doran, G. B., Eldering, A., Fisher, B. M., Fu, D., Gunson, M. R., Mandrake, L., Osterman, G. B., Schwandner, F. M., Sun, K., Taylor, T. E., Wennberg, P. O., and Wunch, D.: The on-orbit performance of the Orbiting Carbon Observatory-2 (OCO-2) instrument and its radiometrically calibrated products, *Atmos. Meas. Tech.*, 10, 59–81, <https://doi.org/10.5194/amt-10-59-2017>, 2017.

Crowell, S., Baker, D., Schuh, A., Basu, S., Jacobson, A. R., Chevallier, F., Liu, J., Deng, F., Feng, L., McKain, K., Chatterjee, A., Miller, J. B., Stephens, B. B., Eldering, A., Crisp, D., Schimel, D., Nassar, R., O'Dell, C. W., Oda, T., Sweeney, C., Palmer, P. I., and Jones, D. B. A.: The 2015–

Deleted: ¶

Formatted: Font: (Default) Times New Roman, 12 pt

Formatted: Justified

Formatted: Font: (Default) Times New Roman, 12 pt

2016 carbon cycle as seen from OCO-2 and the global in situ network, *Atmos. Chem. Phys.*, 19, 9797–9831, <https://doi.org/10.5194/acp-19-9797-2019>, 2019.

Falk, M., Wharton, S., Schroeder, M., Ustin, S., and U, K.T.P.: Flux partitioning in an old-growth forest: seasonal and interannual dynamics. *Tree Physiol.*, 28, 509–520, <https://doi.org/10.1093/treephys/28.4.509>, 2008.

[Fisher, M. and Courtier, P. \(1995\) Estimating the covariance matrices of analysis and forecast error in variational data assimilation. Technical Memorandum 220. Reading, UK: ECMWF.](#)

Friedlingstein, P., Meinshausen, M., Arora, V.K., Jones, C.D., Anav, A., Liddicoat, S.K., and Knutti, R.: Uncertainties in CMIP5 climate projections due to carbon cycle feedbacks, *J. Clim.*, 27, 511–526, <https://doi.org/10.1175/JCLI-D-12-00579.1>, 2014.

Friedlingstein, P., Jones, M., O'Sullivan, M., Andrew, R., Hauck, J., Peters, G., Peters, W., Pongratz, J., Sitch, S., Le Quéré, C., and DBakker, O.: Global carbon budget 2019, *Earth Syst. Sci. Data*, 11, 1783–1838, <https://doi.org/10.3929/ethz-b-000385668>, 2019.

Gatti, L.V., Gloor, M., Miller, J.B., Doughty, C.E., Malhi, Y., Domingues, L.G., Basso, L.S., Martinewski, A., Correia, C.S.C., Borges, V.F., and Freitas, S., 2014, Drought sensitivity of Amazonian carbon balance revealed by atmospheric measurements, *Nature*, 506, 76–80, <https://doi.org/10.1038/nature12957>, 2014.

Gaubert, B., Stephens, B. B., Basu, S., Chevallier, F., Deng, F., Kort, E. A., Patra, P. K., Peters, W., Rödenbeck, C., Saeki, T., Schimel, D., Van der Laan-Luijkx, I., Wofsy, S., and Yin, Y.: Global atmospheric CO<sub>2</sub> inverse models converging on neutral tropical land exchange, but disagreeing on fossil fuel and atmospheric growth rate, *Biogeosciences*, 16, 117–134, <https://doi.org/10.5194/bg-16-117-2019>, 2019.

Gurney, K.R., Law, R.M., Denning, A.S., Rayner, P.J., Pak, B.C., Baker, D., Bousquet, P., Bruhwiler, L., Chen, Y.H., Ciais, P., and Fung, I.Y.: Transcom 3 inversion intercomparison: Model mean results for the estimation of seasonal carbon sources and sinks, *Global Biogeochem. Cycles*, 18, GB1010, <https://doi.org/10.1029/2003GB002111>, 2004.

Henze, D. K., Hakami, A., and Seinfeld, J. H.: Development of the adjoint of GEOS-Chem, *Atmos. Chem. Phys.*, 7, 2413–2433, <https://doi.org/10.5194/acp-7-2413-2007>, 2007.

Jiang, Z., Worden, J. R., Worden, H., Deeter, M., Jones, D. B. A., Arellano, A. F., and Henze, D. K.: A 15-year record of CO emissions constrained by MOPITT CO observations, *Atmos. Chem. Phys.*, 17, 4565–4583, <https://doi.org/10.5194/acp-17-4565-2017>, 2017.

Joiner, J., Guanter, L., Lindstrot, R., Voigt, M., Vasilkov, A. P., Middleton, E. M., Huemmrich, K. F., Yoshida, Y., and Frankenberg, C.: Global monitoring of terrestrial chlorophyll fluorescence from moderate-spectral-resolution near-infrared satellite measurements: methodology,

Formatted: Font: (Default) Times New Roman, 12 pt

Formatted: Font: (Default) Times New Roman, 12 pt, Not Italic

Formatted: Font: (Default) Times New Roman, 12 pt



simulations, and application to GOME-2, *Atmos. Meas. Tech.*, 6, 2803–2823, <https://doi.org/10.5194/amt-6-2803-2013>, 2013.

Joiner, J., Yoshida, Y., Zhang, Y., Duveiller, G., Jung, M., Lyapustin, A., Wang, Y., & Tucker, C.: Estimation of terrestrial global gross primary production (GPP) with satellite data-driven models and eddy covariance flux data. *Remote Sensing*, 10(9), 1346. <https://doi.org/10.3390/rs10091346>. 2018.

Jones, D. B. A., Bowman, K. W., Logan, J. A., Heald, C. L., Liu, J., Luo, M., Worden, J., and Drummond, J.: The zonal structure of tropical O<sub>3</sub> and CO as observed by the Tropospheric Emission Spectrometer in November 2004 – Part 1: Inverse modeling of CO emissions, *Atmos. Chem. Phys.*, 9, 3547–3562, <https://doi.org/10.5194/acp-9-3547-2009>, 2009.

Kiel, M., O'Dell, C. W., Fisher, B., Eldering, A., Nassar, R., MacDonald, C. G., and Wennberg, P. O.: How bias correction goes wrong: measurement of X<sub>CO<sub>2</sub></sub> affected by erroneous surface pressure estimates, *Atmos. Meas. Tech.*, 12, 2241–2259, <https://doi.org/10.5194/amt-12-2241-2019>, 2019.

Konings, A. G., Bloom, A. A., Liu, J., Parazoo, N. C., Schimel, D. S., and Bowman, K. W.: Global satellite-driven estimates of heterotrophic respiration, *Biogeosciences*, 16, 2269–2284, <https://doi.org/10.5194/bg-16-2269-2019>, 2019.

Kulawik, S. S., Crowell, S., Baker, D., Liu, J., McKain, K., Sweeney, C., Biraud, S. C., Wofsy, S., O'Dell, C. W., Wennberg, P. O., Wunch, D., Roehl, C. M., Deutscher, N. M., Kiel, M., Griffith, D. W. T., Velazco, V. A., Notholt, J., Warneke, T., Petri, C., De Mazière, M., Sha, M. K., Sussmann, R., Rettinger, M., Pollard, D. F., Morino, I., Uchino, O., Hase, F., Feist, D. G., Roche, S., Strong, K., Kivi, R., Iraci, L., Shiomi, K., Dubey, M. K., Sepulveda, E., Rodriguez, O. E. G., Té, Y., Jeseck, P., Heikkinen, P., Dlugokencky, E. J., Gunson, M. R., Eldering, A., Crisp, D., Fisher, B., and Osterman, G. B.: Characterization of OCO-2 and ACOS-GOSAT biases and errors for CO<sub>2</sub> flux estimates, *Atmos. Meas. Tech. Discuss.*, <https://doi.org/10.5194/amt-2019-257>, in review, 2019.

Kuze, A., Suto, H., Shiomi, K., Kawakami, S., Tanaka, M., Ueda, Y., Deguchi, A., Yoshida, J., Yamamoto, Y., Kataoka, F., Taylor, T. E., and Buijs, H. L.: Update on GOSAT TANSO-FTS performance, operations, and data products after more than 6 years in space, *Atmos. Meas. Tech.*, 9, 2445–2461, <https://doi.org/10.5194/amt-9-2445-2016>, 2016.

Le Quéré, C., Andrew, R. M., Friedlingstein, P., Sitch, S., Pongratz, J., Manning, A. C., Korsbakken, J. I., Peters, G. P., Canadell, J. G., Jackson, R. B., Boden, T. A., Tans, P. P., Andrews, O. D., Arora, V. K., Bakker, D. C. E., Barbero, L., Becker, M., Betts, R. A., Bopp, L., Chevallier, F., Chini, L. P., Ciais, P., Cosca, C. E., Cross, J., Currie, K., Gasser, T., Harris, I., Hauck, J., Haverd, V., Houghton, R. A., Hunt, C. W., Hurtt, G., Ilyina, T., Jain, A. K., Kato, E., Kautz, M., Keeling, R. F., Klein Goldewijk, K., Körtzinger, A., Landschützer, P., Lefèvre, N., Lenton, A., Lienert, S., Lima, I., Lombardozzi, D., Metzl, N., Millero, F., Monteiro, P. M. S., Munro, D. R., Nabel, J. E. M. S., Nakaoka, S., Nojiri, Y., Padin, X. A., Peregon, A., Pfeil, B., Pierrot, D., Poulter, B., Rehder, G., Reimer, J., Rödenbeck, C., Schwinger, J., Séférian, R., Skjelvan, I., Stocker, B. D., Tian, H., Tilbrook, B., Tubiello, F. N., van der Laan-Luijkx, I. T., van der Werf, G. R., van Heuven, S.,

**Deleted:**

Keppel-Aleks, G., Wennberg, P. O., Washenfelder, R. A., Wunch, D., Schneider, T., Toon, G. C., Andres, R. J., Blavier, J.-F., Connor, B., Davis, K. J., Desai, A. R., Messerschmidt, J., Notholt, J., Roehl, C. M., Sherlock, V., Stephens, B. B., Vay, S. A., and Wofsy, S. C.: The imprint of surface fluxes and transport on variations in total column carbon dioxide, *Biogeosciences*, 9, 875–891, <https://doi.org/10.5194/bg-9-875-2012>, 2012.

1110 Viovy, N., Vuichard, N., Walker, A. P., Watson, A. J., Wiltshire, A. J., Zaehle, S., and Zhu, D.:  
 1111 Global Carbon Budget 2017, *Earth Syst. Sci. Data*, 10, 405–448, [https://doi.org/10.5194/essd-10-](https://doi.org/10.5194/essd-10-405-2018)  
 1112 405-2018, 2018.  
 1113  
 1114 Liu, J., Baskarran, L., Bowman, K., Schimel, D., Bloom, A. A., Parazoo, N., Oda, T., Carrol, D.,  
 1115 Menemenlis, D., Joiner, J., Commane, R., Daube, B., Gatti, L. V., McKain, K., Miller, J.,  
 1116 Stephens, B. B., Sweeney, C., & Wofsy, S. (2020). *CMS-Flux NBE 2020* [Data set]. NASA.  
 1117 <https://doi.org/10.25966/4V02-C391>  
 1118  
 1119 Liu, J. and Bowman, K.: A method for independent validation of surface fluxes from atmospheric  
 1120 inversion: Application to CO<sub>2</sub>, *Geophys. Res. Lett.*, 43, 3502–3508,  
 1121 <https://doi.org/10.1002/2016GL067828>, 2016.  
 1122  
 1123 Liu, J., Bowman, K. W., and Henze, D. K.: Source-receptor relationships of column-average  
 1124 CO<sub>2</sub> and implications for the impact of observations on flux inversions. *J. Geophys. Res.*  
 1125 *Atmos.*, 120, 5214– 5236. doi: [10.1002/2014JD022914](https://doi.org/10.1002/2014JD022914), 2015  
 1126  
 1127 Liu, J., Bowman, K.W., Lee, M., Henze, D.K., Bousserez, N., Brix, H., James Collatz, G.,  
 1128 Menemenlis, D., Ott, L., Pawson, S., and Jones, D.: Carbon monitoring system flux estimation and  
 1129 attribution: impact of ACOS-GOSAT XCO<sub>2</sub> sampling on the inference of terrestrial biospheric  
 1130 sources and sinks. *Tellus B Chem. Phys. Meteorol.* B., 66, 22486,  
 1131 <http://dx.doi.org/10.3402/tellusb.v66.22486>, 2014.  
 1132  
 1133 Liu, J., Bowman, K.W., Schimel, D.S., Parazoo, N.C., Jiang, Z., Lee, M., Bloom, A.A., Wunch,  
 1134 D., Frankenberg, C., Sun, Y., and O'Dell, C.W.: Contrasting carbon cycle responses of the tropical  
 1135 continents to the 2015–2016 El Niño. *Science*, 358, eaam5690,  
 1136 <https://doi.org/10.1126/science.aam5690>, 2017.  
 1137  
 1138 Liu, J., Bowman, K., Parazoo, N.C., Bloom, A.A., Wunch, D., Jiang, Z., Gurney, K.R., and  
 1139 Schimel, D.: Detecting drought impact on terrestrial biosphere carbon fluxes over contiguous US  
 1140 with satellite observations. *Environ. Res. Lett.*, 13, 095003, [https://doi.org/10.1088/1748-](https://doi.org/10.1088/1748-9326/aad5ef)  
 1141 9326/aad5ef, 2018.  
 1142  
 1143 [Liu, Z.-Q. and Rabier, F. \(2003\). The potential of high-density observations for numerical](#)  
 1144 [weather prediction: A study with simulated observations. Q.J.R. Meteorol. Soc., 129: 3013-3035.](#)  
 1145 [doi:10.1256/qj.02.170](#)  
 1146  
 1147  
 1148 [Lorenc, A. C., 1981: A Global Three-Dimensional Multivariate Statistical Interpolation](#)  
 1149 [Scheme. Mon. Wea. Rev., 109, 701–721](#)  
 1150  
 1151  
 1152 Lovenduski, N.S. and Bonan, G.B.: Reducing uncertainty in projections of terrestrial carbon  
 1153 uptake, *Environ. Res. Lett.*, 12, 044020, <https://doi.org/10.1088/1748-9326/aa66b8>, 2017.  
 1154

Formatted: Font: (Default) Times New Roman, 12 pt

Formatted: Font: (Default) Times New Roman, 12 pt

Formatted: Font: Times New Roman

Deleted: ¶

1156 [Meirink, J.F., Bergamaschi, P. and Krol, M.C. \(2008\) Four-dimensional variational data](#)  
1157 [assimilation for inverse modelling of atmospheric methane emissions: method and comparison](#)  
1158 [with synthesis inversion, \*Atmos. Chem. Phys.\*, \*\*8\*\*, 6341–6353, \[https://doi.org/10.5194/acp-8-\]\(https://doi.org/10.5194/acp-8-6341-2008\)](#)  
1159 [6341-2008.](#)

Formatted: Font: (Default) Times New Roman, 12 pt

Formatted: Justified

1160  
1161 Nassar, R., Jones, D.B., Suntharalingam, P., Chen, J.M., Andres, R.J., Wecht, K.J., Yantosca, R.M.,  
1162 Kulawik, S.S., Bowman, K.W., Worden, J.R., and Machida, T.: Modeling global atmospheric CO<sub>2</sub>  
1163 with improved emission inventories and CO<sub>2</sub> production from the oxidation of other carbon  
1164 species. *Geosci. Model Dev.*, 3, 689–716, <https://doi.org/10.5194/gmd-3-689-2010>, 2010.

1165  
1166 [Niwa, Y., Fujii, Y. A conjugate BFGS method for accurate estimation of a posterior error](#)  
1167 [covariance matrix in a linear inverse problem. \*Q J R Meteorol\*](#)  
1168 [Soc.](#) 2020; 1– 26. <https://doi.org/10.1002/qj.3838>

Formatted: Font: (Default) Times New Roman, 12 pt

Formatted: Justified

Formatted: Font: (Default) Times New Roman, 12 pt

1170 Oda, T., Maksyutov, S., and Andres, R. J.: The Open-source Data Inventory for Anthropogenic  
1171 CO<sub>2</sub>, version 2016 (ODIAC2016): a global monthly fossil fuel CO<sub>2</sub> gridded emissions data product  
1172 for tracer transport simulations and surface flux inversions, *Earth Syst. Sci. Data*, 10, 87–107,  
1173 <https://doi.org/10.5194/essd-10-87-2018>, 2018.

1174  
1175 O'Dell, C. W., Connor, B., Bösch, H., O'Brien, D., Frankenberg, C., Castano, R., Christi, M.,  
1176 Eldering, D., Fisher, B., Gunson, M., McDuffie, J., Miller, C. E., Natraj, V., Oyafuso, F., Polonsky,  
1177 I., Smyth, M., Taylor, T., Toon, G. C., Wennberg, P. O., and Wunch, D.: The ACOS CO<sub>2</sub> retrieval  
1178 algorithm – Part 1: Description and validation against synthetic observations, *Atmos. Meas. Tech.*,  
1179 5, 99–121, <https://doi.org/10.5194/amt-5-99-2012>, 2012.

1180  
1181 O'Dell, C., Eldering, A., Wennberg, P.O., Crisp, D., Gunson, M., Fisher, B., Frankenberg, C., Kiel,  
1182 M., Lindqvist, H., Mandrake, L., and Merrelli, A.: Improved retrievals of carbon dioxide from  
1183 Orbiting Carbon Observatory-2 with the version 8 ACOS algorithm, *Atmos. Meas. Tech.*, 11,  
1184 6539–6576, <https://doi.org/10.5194/amt-11-6539-2018>, 2018.

1185  
1186 Olsen, S.C. and Randerson, J.T.: Differences between surface and column atmospheric CO<sub>2</sub> and  
1187 implications for carbon cycle research, *J. Geophys. Res: Atmos.*, 109, D02301,  
1188 <https://doi.org/10.1029/2003JD003968>, 2004.

1189  
1190 Parazoo, N.C., Bowman, K., Fisher, J.B., Frankenberg, C., Jones, D.B.A., Cescatti, A., Pérez-  
1191 Priego, Ó., Wohlfahrt, G. and Montagnani, L.: Terrestrial gross primary production inferred from  
1192 satellite fluorescence and vegetation models. *Glob Change Biol*, 20: 3103–3121.  
1193 doi:[10.1111/gcb.12652](https://doi.org/10.1111/gcb.12652). 2014.

1194  
1195 [Peylin, P., Law, R. M., Gurney, K. R., Chevallier, F., Jacobson, A. R., Maki, T., Niwa, Y., Patra,](#)  
1196 [P. K., Peters, W., Rayner, P. J., Rödenbeck, C., van der Laan-Luijkx, I. T., and Zhang, X.: Global](#)  
1197 [atmospheric carbon budget: results from an ensemble of atmospheric CO<sub>2</sub> inversions,](#)  
1198 [\*Biogeosciences\*, \*\*10\*\*, 6699–6720, <https://doi.org/10.5194/bg-10-6699-2013>, 2013.](#)

Formatted: Font: Times New Roman, 12 pt

Formatted: Justified

1201 [Peters, W., et al. \(2007\). An atmospheric perspective on North American carbon dioxide exchange](#)  
 1202 [CarbonTracker, \*Proc. Natl. Acad. Sci. U. S. A.\*, \*\*104\*\*\(48\), 18,925– 18,930,](#)  
 1203 [doi:10.1073/pnas.0708986104.](#)

1204

1205 [Peters, W., Krol, M. C., Van Der Werf, G.R., et al, 2010, Seven years of recent European net](#)  
 1206 [terrestrial carbon dioxide exchange constrained by atmospheric observations. \*Global Change\*](#)  
 1207 [Biology, \*\*16\*\*: 1317-1337. doi:10.1111/j.1365-2486.2009.02078.x](#)

1208

1209

1210 Poulter, B., Frank, D., Ciais, P., Myneni, R.B., Andela, N., Bi, J., Broquet, G., Canadell, J.G.,  
 1211 Chevallier, F., Liu, Y.Y., and Running, S.W.: Contribution of semi-arid ecosystems to interannual  
 1212 variability of the global carbon cycle, *Nature*, 509, 600-603, <https://doi.org/10.1038/nature13376>,  
 1213 2014.

1214

1215 Quetin, G., Bloom, A. A., Bowman, K. W., & Konings, A.: Carbon flux variability from a  
 1216 relatively simple ecosystem model with assimilated data is consistent with terrestrial biosphere  
 1217 model estimates. *Journal of Advances in Modeling Earth Systems*, 12,  
 1218 e2019MS001889. <https://doi.org/10.1029/2019MS001889>, 2020

1219

1220 Randerson, J.T., Van Der Werf, G.R., Giglio, L., Collatz, G.J., and Kasibhatla, P.S.: Global Fire  
 1221 Emissions Database, Version 4.1 (GFEDv4), ORNL DAAC, Oak Ridge, Tennessee,  
 1222 USA, <https://doi.org/10.3334/ORNLDAAAC/1293>, 2018.

1223

1224 Rienecker, M.M., Suarez, M.J., Gelaro, R., Todling, R., Bacmeister, J., Liu, E., Bosilovich, M.G.,  
 1225 Schubert, S.D., Takacs, L., Kim, G.K., and Bloom, S.: MERRA: NASA's modern-era  
 1226 retrospective analysis for research and applications, *J. Clim.*, 24, 3624-3648,  
 1227 <https://doi.org/10.1175/JCLI-D-11-00015.1>, 2011.

1228

1229 [Rödenbeck, C., Houweling, S., Gloor, M., and Heimann, M.: CO<sub>2</sub> flux history 1982–2001 inferred](#)  
 1230 [from atmospheric data using a global inversion of atmospheric transport, \*Atmos. Chem. Phys.\*, \*\*3\*\*,](#)  
 1231 [1919–1964, <https://doi.org/10.5194/acp-3-1919-2003>, 2003.](#)

1232

1233

1234 Running, S.W., Baldocchi, D.D., Turner, D.P., Gower, S.T., Bakwin, P.S., and Hibbard, K.A.: A  
 1235 global terrestrial monitoring network integrating tower fluxes, flask sampling, ecosystem  
 1236 modeling and EOS satellite data, *Remote Sens. Environ.*, 70, 108-127,  
 1237 [https://doi.org/10.1016/S0034-4257\(99\)00061-9](https://doi.org/10.1016/S0034-4257(99)00061-9), 1999.

1238

1239 Schuh, A.E., Jacobson, A.R., Basu, S., Weir, B., Baker, D., Bowman, K., Chevallier, F., Crowell,  
 1240 S., Davis, K.J., Deng, F., and Denning, S.: Quantifying the impact of atmospheric transport  
 1241 uncertainty on CO<sub>2</sub> surface flux estimates, *Global Biogeochem. Cy.*, 33, 484-500,  
 1242 <https://doi.org/10.1029/2018GB006086>, 2019.

1243

1244 Sellers, P.J., Schimel, D.S., Moore, B., Liu, J., and Eldering, A.: Observing carbon cycle–climate  
 1245 feedbacks from space, *PNAS*, 115, 7860-7868, <https://doi.org/10.1073/pnas.1716613115>, 2018.

1246

Formatted: Font: (Default) Times New Roman, 12 pt

Formatted: Justified

Formatted: Font: (Default) Times New Roman, 12 pt

Formatted: Font: (Default) Times New Roman, 12 pt

Formatted: Font: (Default) Times New Roman

Formatted: Font: (Default) Times New Roman

Formatted: Font: (Default) Times New Roman, 12 pt

Formatted: Font: (Default) Times New Roman, 12 pt

Formatted: Font: Times New Roman, 12 pt

Formatted: Justified

1247 Stephens, B.B., Gurney, K. R., Tans, P. P., *et al.*: Weak northern and strong tropical land carbon  
 1248 uptake from vertical profiles of atmospheric CO<sub>2</sub>. *Science* **316**: 1732– 35,  
 1249 doi:10.1126/science.1137004. 2007  
 1250  
 1251 Stephens, B., et al. 2017. ORCAS Airborne Oxygen Instrument. Version 1.0. UCAR/NCAR -  
 1252 Earth Observing Laboratory. <https://doi.org/10.5065/D6N29VC6>.

1253 Sweeney, C., Karion, A., Wolter, S., et al.: Seasonal climatology of CO<sub>2</sub> across North America  
 1254 from aircraft measurements in the NOAA/ESRL Global Greenhouse Gas Reference Network. *J.*  
 1255 *Geophys. Res. Atmos.*, 120, 5155– 5190. doi: [10.1002/2014JD022591](https://doi.org/10.1002/2014JD022591). 2015

1256  
 1257 Suntharalingam, P., Jacob, D.J., Palmer, P.I., Logan, J.A., Yantosca, R.M., Xiao, Y., Evans, M.J.,  
 1258 Streets, D.G., Vay, S.L., and Sachse, G.W.: Improved quantification of Chinese carbon fluxes  
 1259 using CO<sub>2</sub>/CO correlations in Asian outflow, *J. Geophys. Res.: Atmos.*, 109, D18S18,  
 1260 <https://doi.org/10.1029/2003JD004362>, 2004.  
 1261  
 1262 Tramontana, G., Jung, M., Schwalm, C. R., Ichii, K., Camps-Valls, G., Ráduly, B., Reichstein, M.,  
 1263 Arain, M. A., Cescatti, A., Kiely, G., Merbold, L., Serrano-Ortiz, P., Sickert, S., Wolf, S., and  
 1264 Papale, D.: Predicting carbon dioxide and energy fluxes across global FLUXNET sites with  
 1265 regression algorithms, *Biogeosciences*, 13, 4291–4313, <https://doi.org/10.5194/bg-13-4291-2016>,  
 1266 2016.  
 1267  
 1268 [van der Laan-Luijkx et al. 2017, "The CarbonTracker Data Assimilation Shell \(CTDAS\) v1.0:  
 1269 implementation and global carbon balance 2001-2015", \*Geosci. Model Dev.\*, 10, 2785-2800.](#)  
 1270  
 1271 van der Werf, G. R., Randerson, J. T., Giglio, L., Gobron, N., and Dolman, A. J.: Climate  
 1272 controls on the variability of fires in the tropics and subtropics, *Global Biogeochem. Cycles*, 22,  
 1273 GB3028, doi:10.1029/2007GB003122. 2008  
 1274  
 1275  
 1276  
 1277 Wofsy, S. C.: HIPER Pole-to-Pole Observations (HIPPO): Fine-grained, global-scale  
 1278 measurements of climatically important atmospheric gases and aerosols, *Philos. Trans. R. Soc. A-*  
 1279 *Math. Phys. Eng. Sci.*, 369, 2073– 2086, <https://doi.org/10.1098/rsta.2010.0313>, 2011.  
 1280  
 1281 Wofsy, S.C., Afshar, S., Allen, H.M., Apel, E., Asher, E.C., Barletta, B., Bent, J., Bian, H., Biggs,  
 1282 B.C., Blake, D.R., and Blake, N.: ATom: Merged Atmospheric Chemistry, Trace Gases, and  
 1283 Aerosols, ORNL DAAC, Oak Ridge, Tennessee,  
 1284 USA, <https://doi.org/10.3334/ORNLDAAAC/1581>, 2018.  
 1285  
 1286 Wunch, D., Toon, G.C., Blavier, J.F.L., Washenfelder, R.A., Notholt, J., Connor, B.J., Griffith,  
 1287 D.W., Sherlock, V., and Wennberg, P.O.: The total carbon column observing network, *Philos.*  
 1288 *Trans. R. Soc. A*, 369, 2087-2112, <https://doi.org/10.1098/rsta.2010.0240>, 2011.  
 1289

Formatted: Font: (Default) Times New Roman

Formatted: Justified

Formatted: Font: (Default) Times New Roman, Not Bold

1290 Yin, Y., Bowman, K., Bloom, A.A., and Worden, J.: Detection of fossil fuel emission trends in the  
1291 presence of natural carbon cycle variability, *Environ. Res. Lett.*, 14, 084050,  
1292 <https://doi.org/10.1088/1748-9326/ab2dd7>, 2019.

1293  
1294 Zhu, C., Byrd, R.H., Lu, P., and Nocedal, J.: Algorithm 778: L-BFGS-B: Fortran subroutines for  
1295 large-scale bound-constrained optimization, *ACM Trans. Math. Softw.*, 23, 550-560,  
1296 <https://doi.org/10.1145/279232.279236>, 1997.

1297  
1298  
1299

**Deleted:** Yang, Z., Washenfelder, R. A., Keppel-Aleks, G.,  
Krakauer, N. Y., Randerson, J. T., Tans, P. P., Sweeney, C.,  
and Wennberg, P. O.: New constraints on Northern  
Hemisphere growing season net flux, *Geophys. Res.  
Lett.*, 34, L12807, <https://doi.org/10.1029/2007GL029742>,  
2007.

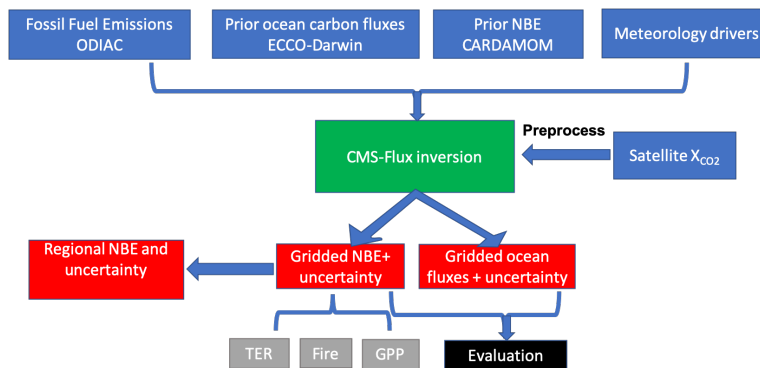


**Figure: 1 Data flow diagram with the main processing steps to generate regional net biosphere change (NBE). TER: total ecosystem respiration; GPP: gross primary production. The green box is the inversion system. The blue boxes are the inputs for the inversion system. The red boxes are the data outputs from the system. The black box is the evaluation step, and the grey boxes are the future additions to the product.**

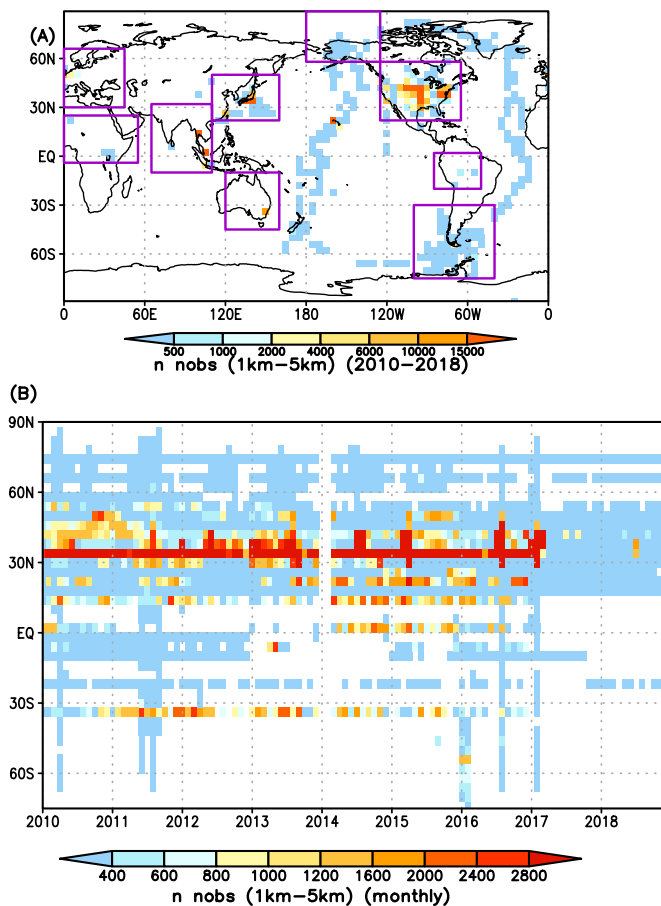
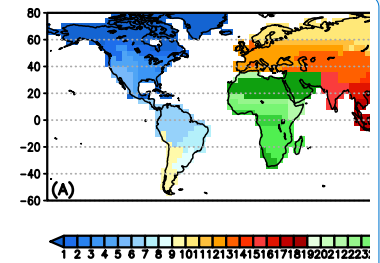
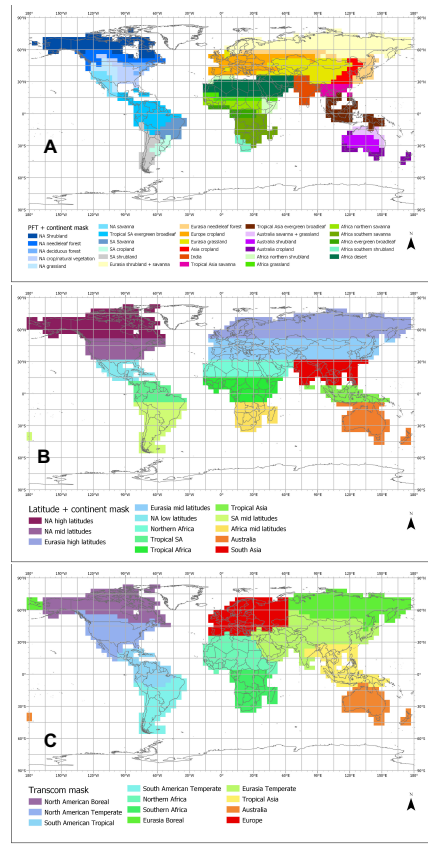


**Figure: 2** The spatial and temporal distributions of aircraft observations used in evaluation of posterior NBE. (A) The total number of aircraft observations between 1–5 km between 2010–2018 at each  $4^\circ \times 5^\circ$  grid point. The rectangle boxes show the range of the nine sub regions. (B) The total number of monthly aircraft observations at each longitude as a function of time.





**Deleted:**

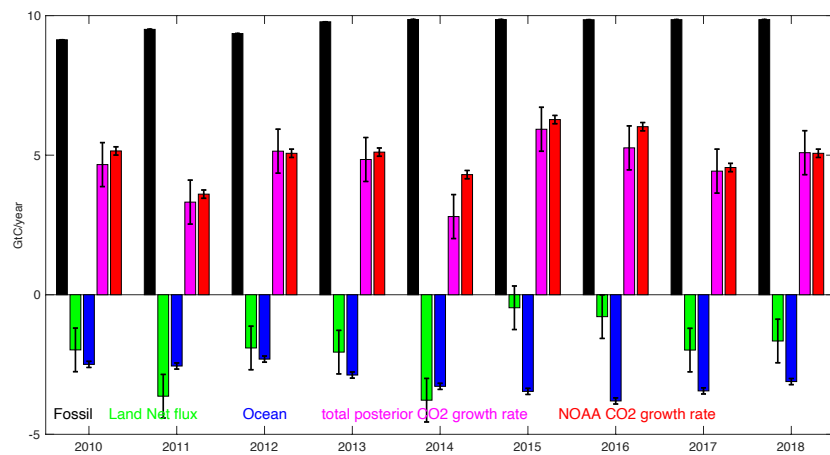
**Formatted: Centered**

Figure: 3 [Three](#) types of regional masks used in calculating regional fluxes. The mask in [the top panel](#) is based on a combination of condensed seven MODIS IGBP plant functional types, TRANCOM-3 regions (Gurney et al., 2004), and continents. The mask in [the middle panel](#) is based on latitude and continents. [The mask in the bottom panel is the TransCom region mask.](#)

**Deleted: Two**

**Deleted: (A)**

**Deleted: (B)**



**Figure: 4 Global flux estimation and uncertainties from 2010–2018 (black: fossil fuel; green: posterior land fluxes; blue: ocean fluxes; magenta: estimated CO<sub>2</sub> growth rate; red: the NOAA CO<sub>2</sub> growth rate).**

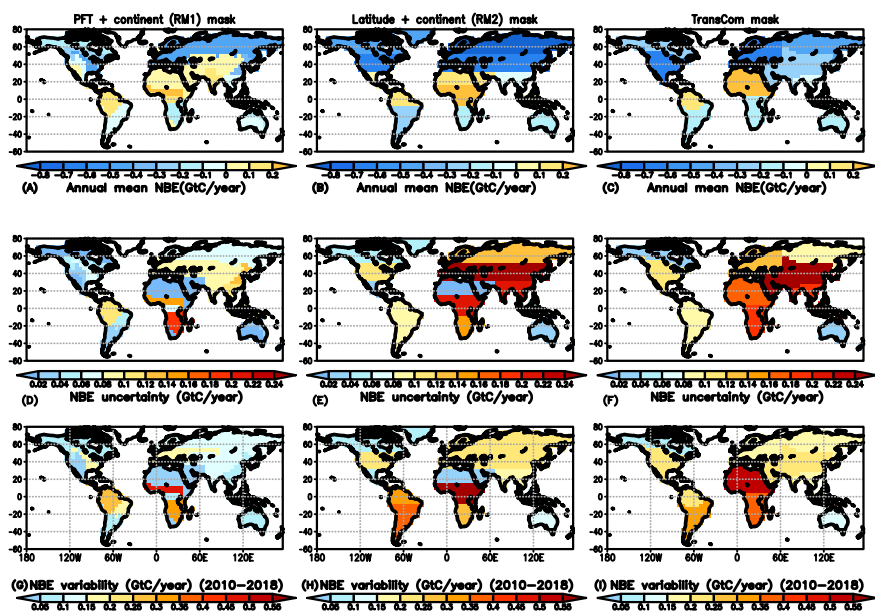
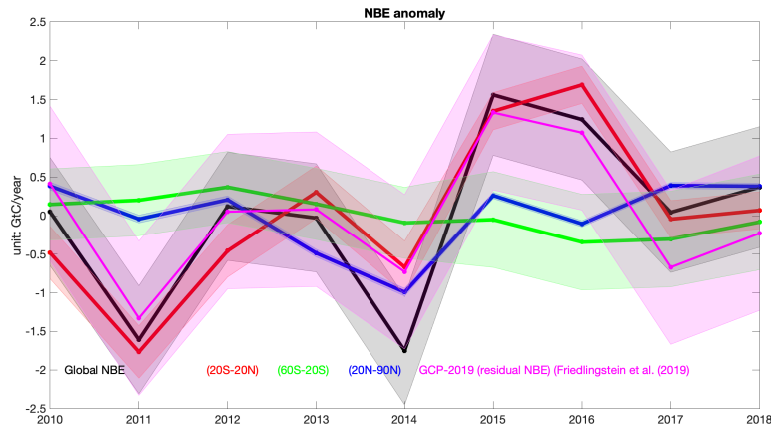


**Figure: 5** Mean annual regional NBE (A, B, and C), uncertainty (D, E, and F), and variability between 2010–2018 (G, H, and I) with the three types of regional masks (Figure 3). The first column uses a region mask based on PFT and continents (RM1). The second column uses a region mask based latitude and continents (RM2), and the third column uses TransCom mask.

1357



1358

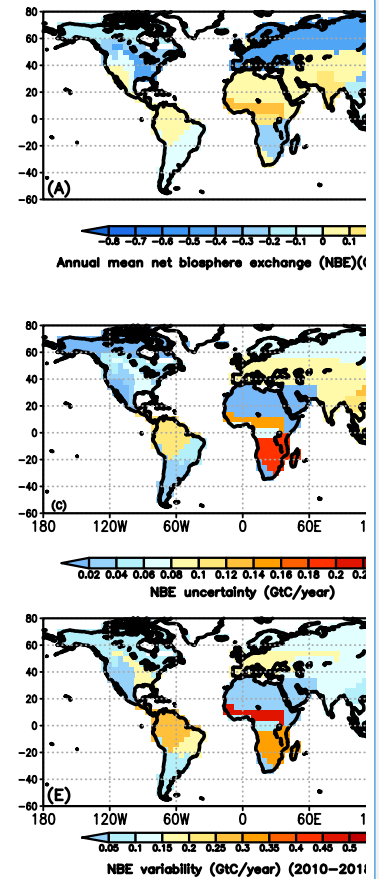
1359 **Figure: 6** The NBE interannual variability over the globe (black), the tropics (20°S–20°N),  
 1360 SH mid-latitudes (60°S–20°S), and NH mid-latitudes (20°N–9°0N). For reference, the  
 1361 residual net land carbon sink from GCP (Friedlingstein et al., 2019) and its uncertainty is  
 1362 also shown (magenta).

1363

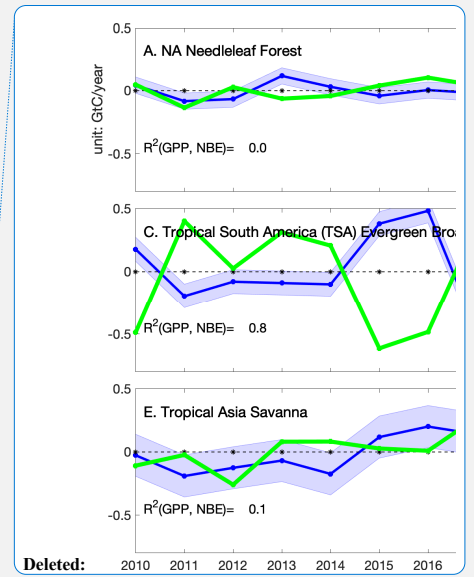
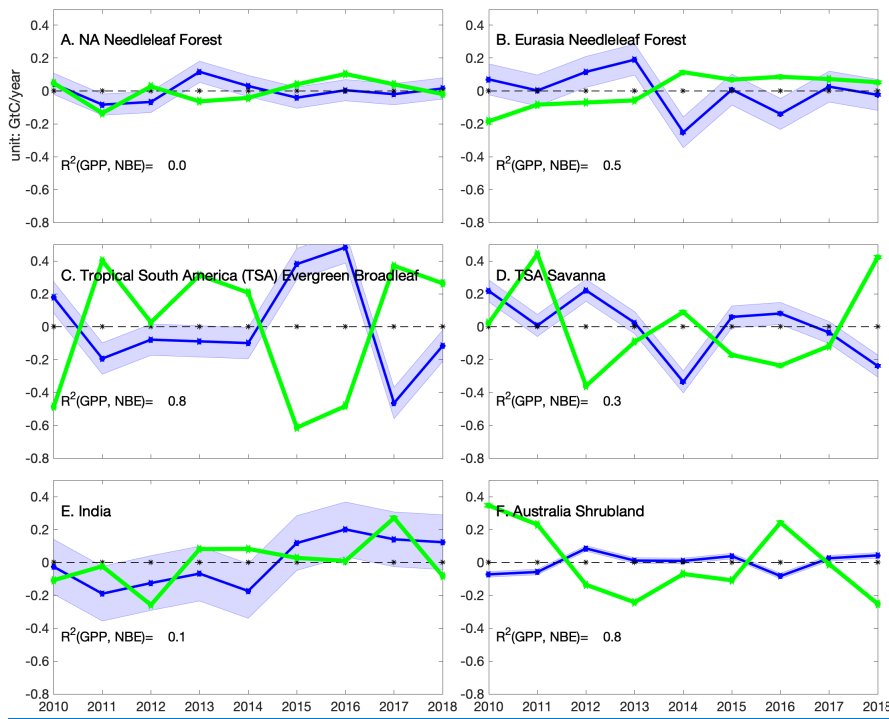
1364

1365

1366



Deleted:  
 Figure: 5 Mean annual regional NBE (A and B),  
 uncertainty (C and D), and variability between 2010–  
 2018 (E and F) with two types of regional masks.



Deleted:

**Figure: 7 The NBE interannual variability over six selected regions. Blue: annual NBE anomaly and its uncertainties. Green: annual GPP anomaly based on FLUXSAT.**

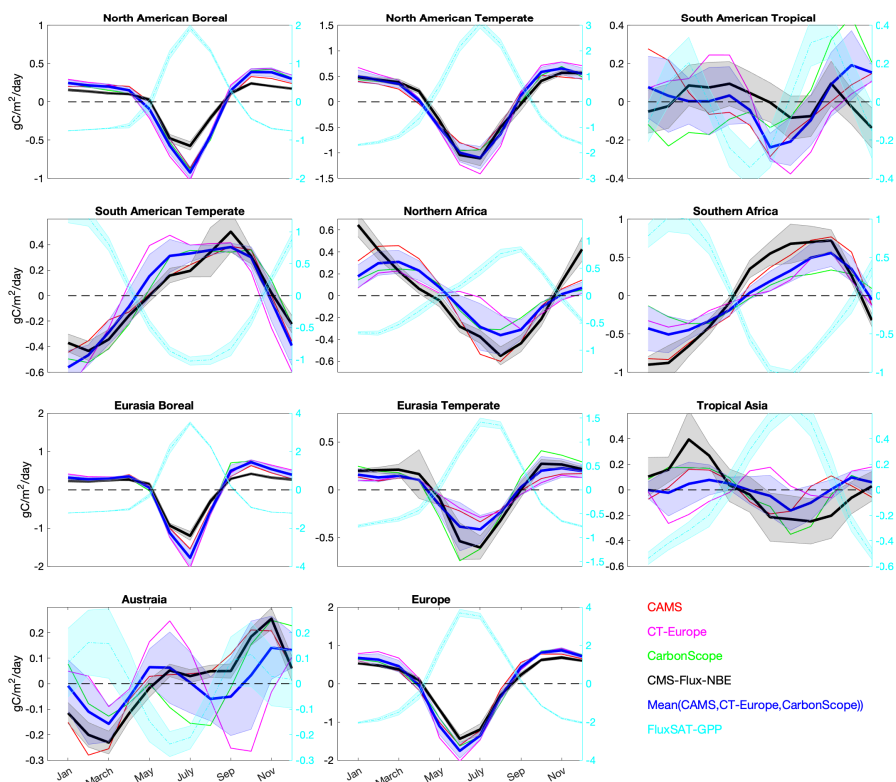
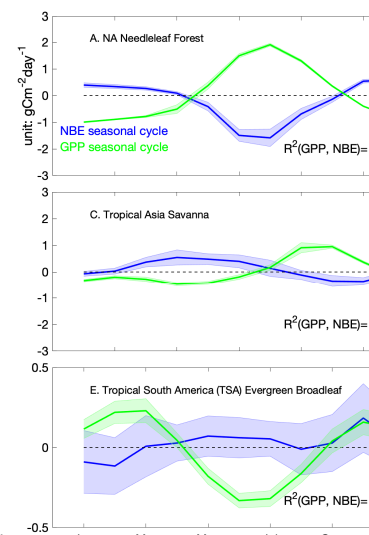


**Figure: 8 The NBE climatological seasonality over TransCom regions. The seasonal cycle is calculated over 2010-2017 since CT-Europe only covers till 2017. Black: CMS-Flux-NBE and its uncertainty; blue shaded: mean NBE seasonality based on surface CO<sub>2</sub> inversion results from CAMS, CT-Europe, and Jena CarbonScope; red: CAMS; magenta: CT-Europe; green: Jena CarbonScope. The names of each region are shown on individual subplots.**



**Deleted:** Figure: 8 Blue: climatological NBE seasonality over six selected regions shown in Figure 3A; blue shaded: NBE monthly uncertainty and variability (1-sigma) over nine years. Green and shaded: monthly mean GPP and its variability (1-sigma) over nine years. The names of each region are shown on individual subplots.

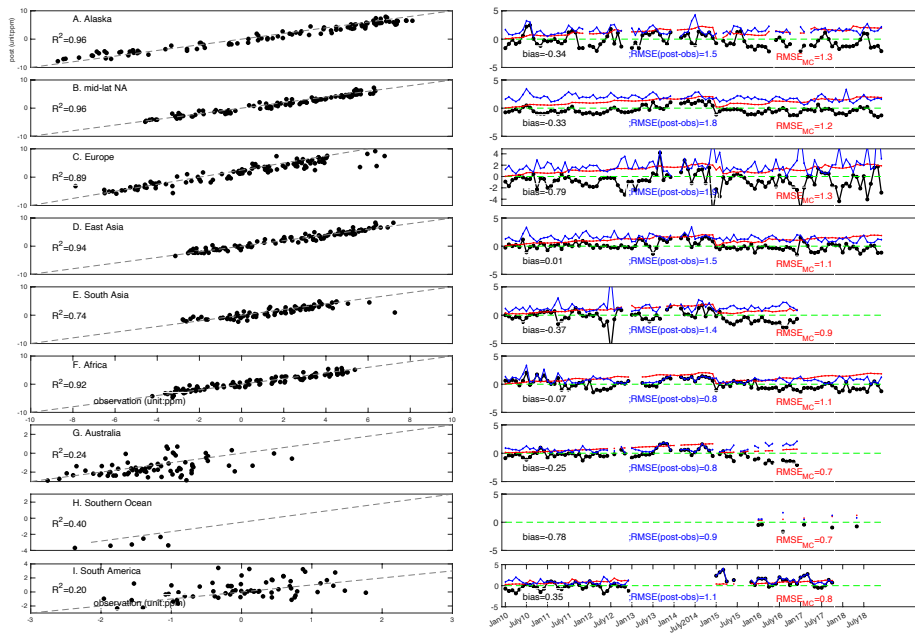
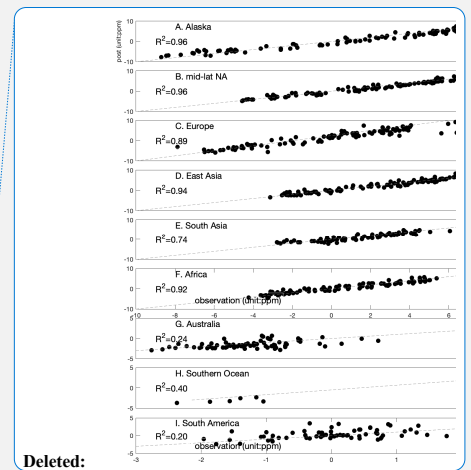


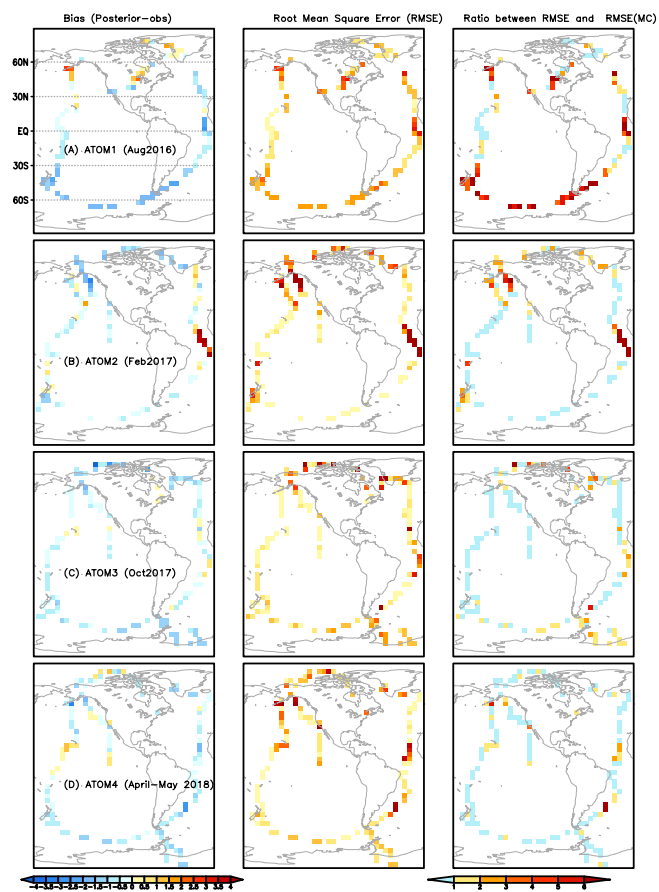
**Figure: 9 Comparison between posterior CO<sub>2</sub> mole fraction and aircraft observations. Left panel: detrended posterior CO<sub>2</sub> (y-axis) vs. detrended aircraft CO<sub>2</sub> (x-axis) over nine regions. The dashed line is 1:1 line; right panel: black: the differences between posterior CO<sub>2</sub> and aircraft CO<sub>2</sub> as a function of time; blue: RMSE (unit: ppm); red: RMSE<sub>MC</sub>.**



Deleted:

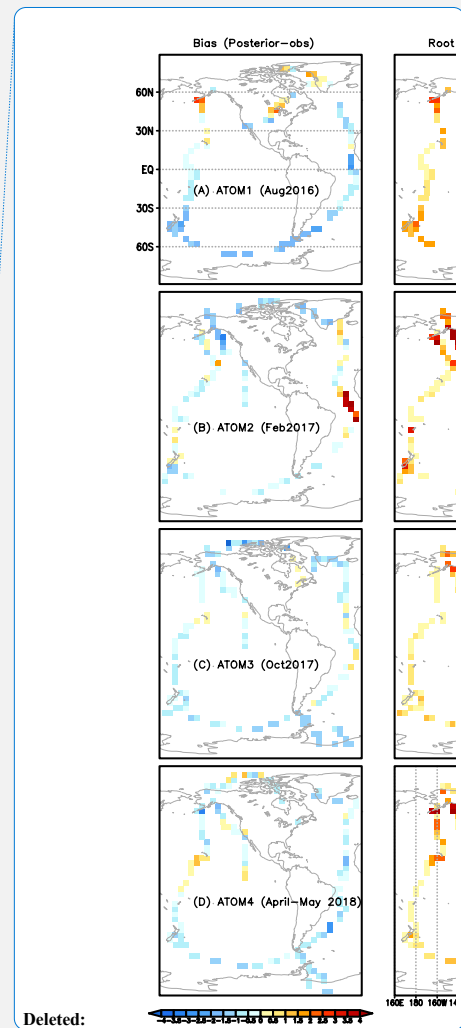
Deleted: The blue bar shows the number of aircraft observations (log scale) as a function of month.

1406  
1407



1408

1409 **Figure: 10** Left column: the mean differences between posterior CO<sub>2</sub> and aircraft  
1410 observations from ATOM 1–4 aircraft campaigns between 1–5 km (A–D). Middle column:  
1411 the Root Mean Square Errors (RMSE) between aircraft observations and posterior CO<sub>2</sub>  
1412 between 1–5 km. The color bar is the same as the left column. Right column: the ratio  
1413 between RMSE and RMSE<sub>MC</sub> based on ensemble CO<sub>2</sub> from the Monte Carlo uncertainty  
1414 estimation method.





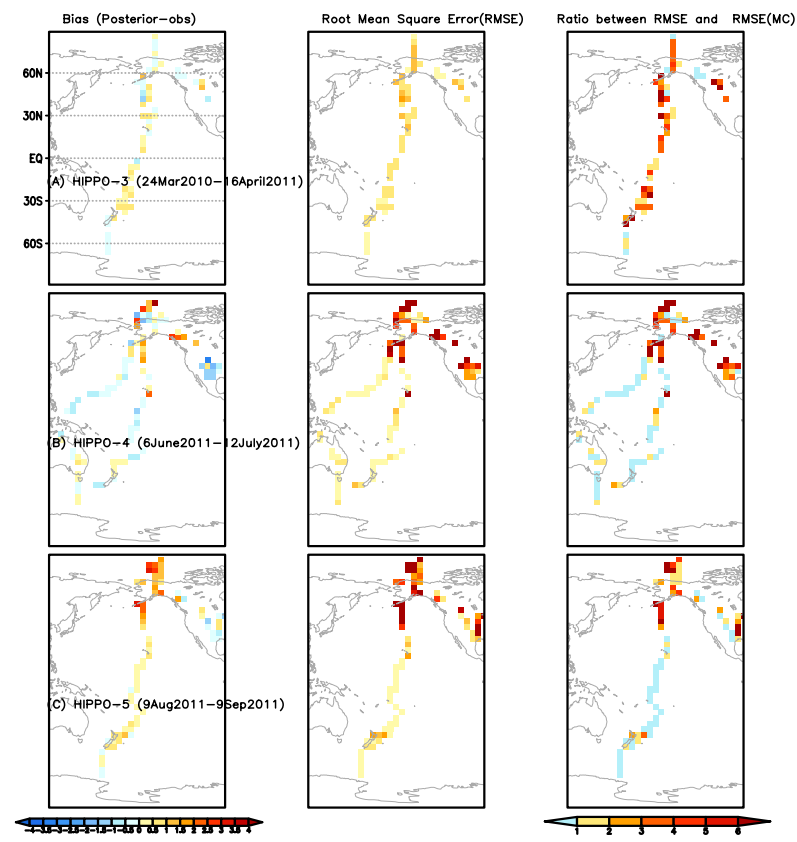
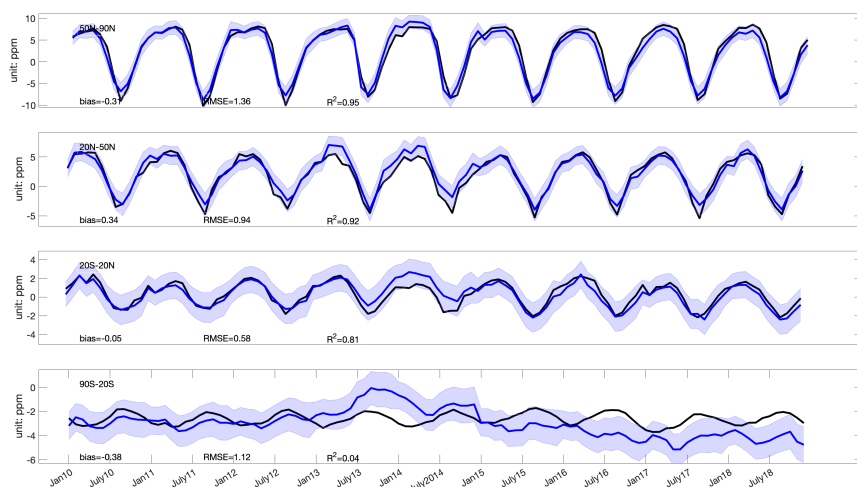


Figure: 11 Left column: the mean differences between posterior CO<sub>2</sub> and aircraft observations from HIPPO 3-5 aircraft campaigns between 1-5 km (A-C) (unit: ppm). The time frame of each campaign is in the figure. Middle column: the Root Mean Square Errors (RMSE) between aircraft observations and posterior CO<sub>2</sub> between 1-5 km (unit: ppm). The color bar is the same as the left column. Right column: the ratio between RMSE and RMSE<sub>MC</sub> based on ensemble CO<sub>2</sub> from the Monte Carlo method.

Deleted:



**Figure: 12 Comparison between posterior CO<sub>2</sub> and the NOAA marine boundary layer (MBL) reference sites. Black: observations averaged over each latitude bands; blue and shaded area: posterior CO<sub>2</sub> and its uncertainty. The global mean CO<sub>2</sub> (<https://www.esrl.noaa.gov/gmd/ccgg/trends/global.html>) was subtracted from both the NOAA MBL reference and posterior CO<sub>2</sub> before the comparison.**

Formatted: Justified

1433  
1434  
1435  
1436  
1437  
1438  
1439

**Table: 1 Configurations of the CMS-Flux atmospheric inversion system**

	Model setup	Configuration	Reference
Inversion general setup	Spatial scale	Global	--
	Spatial resolution	4° latitude x 5° longitude	
	Time resolution	monthly	
	Minimizer of cost function	L-BFGS	Byrd et al., 1994; Zhu et al., 1997
	Control vector	Monthly net terrestrial biosphere fluxes and ocean fluxes	
Transport model	Model name	GEOS-Chem and its adjoint	Suntharalingam et al., 2004 Nassar et al., 2010 Henze et al., 2007
	Meteorological forcing	GEOS-5 (2010–2014) and GEOS-FP (2015–2019)	Rienecker et al., 2008

1440  
1441

1442  
1443

**Table: 2 Description of the prior fluxes and assumed uncertainties in the inversion system**

Prior fluxes	Terrestrial biosphere fluxes	Ocean fluxes	Fossil fuel emissions
Model name	CARDAMOM-v1	ECCO-Darwin	ODIAC 2018
Spatial resolution	4° x 5°	0.5°	1° x 1°
Frequency	3-hourly	3-hourly	hourly
Uncertainty	Estimated from CARDAMOM	100% same as Liu et al. (2017)	No uncertainty
References	Bloom et al., 2006; 2020	Brix et al, 2015; Carroll et al., 2020	Oda et al., 2016; 2018

1444  
  
1445

1446

1447

1448

**Table: 3 Description of observation and evaluation dataset. Data sources are listed in Table 7.**

	Dataset name and version	References
Satellite $X_{CO_2}$	ACOS-GOSAT v7.3	O'Dell et al., (2012)
	OCO-2 v9	O'Dell et al., (2018)
Aircraft $CO_2$ observations	ObsPack OCO-2 MIP	CarbonTracker team (2019)
	HIPPO 3-5	Wofsy et al. (2011)
	ATom 1-4	Wofsy et al. (2018)
	INPE	Gatti et al., (2014)
	ORCAS	Stephens et al. (2017)
NOAA marine boundary layer (MBL) reference	NOAA MBL reference	Conway et al., 1994
GPP	FLUXSAT-GPP	Joiner et al., (2018)
Top-down NBE estimates constrained by surface $CO_2$	CarbonTracker-Europe	van der Laan-Luijkx et al. (2017) Peters et al., (2010) Peters et al. (2007)
	Jena CarbonScope s10oc_v2020	Rödenbeck et al., 2003
	CAMS v18r1	Chevallier et al., 2005

1449

1451  
1452  
1453

Table: 4 Latitude and longitude ranges for seven sub regions.

Region	Alaska	Mid-lat NA	Europe	East Asia	South Asia
Longitude range	180°W–125° W	125°W–65°W	5°W–45°E	110°E–160°E	65°E–110°E
Latitude range	58°N–89°N	22°N–58°N	30°N–66°N	22°N–50°N	10°S–32°N
Region	Africa	South America	Australia	Southern Ocean	
Longitude range	5°W–55°E	95°W–50°W	120°E–160°E	110°W–40°E	
Latitude range	2°N–18°N	20°S–2°N	45°S–10°S	80°S–30°S	

1454  
1455

Deleted: Table: 3 Description of observation and evaluation dataset. Data sources are listed in Table 7. [1]

1458

**Table: 5 List of the data products.**

Deleted: ¶

<u>Product</u>	<u>Spatial resolution</u>	<u>Temporal resolution when applicable</u>	<u>Data format</u>	<u>Sample data description in the text</u>
<u>Total fossil fuel, ocean, and land fluxes</u>	Global	Annual	csv	Figure 4 (section 4.1)
<u>Climatology mean NBE, variability, and uncertainties</u>	PFT and continents based 28 regions	N/A	csv	Figure 5 (section 4.2)
	Geographic-based 13 regions		csv	
	TransCom regions		csv	
<u>Hemispheric NBE and uncertainties</u>	NH (20°N-90°N), tropics (20°S-20°N), and SH (60°S-20°S)	Annual	csv	Figure 6 (section 4.3)
<u>NBE variability and uncertainties</u>	PFT and continents based 28 regions	Annual	csv	Figure 7 (section 4.3)
	Geographic -based 13 regions		csv	
	TransCom regions		csv	
<u>NBE seasonality and its uncertainties</u>	PFT and continents based 28 regions	Monthly	csv	Figure 8 (section 4.4)
	Geographic -based 13 regions		csv	
	TransCom regions		csv	
<u>Monthly NBE and uncertainties</u>	PFT and continents based 28 regions	Monthly	csv	N/A
	Geographic -based 13 regions		csv	
	TransCom		csv	
<u>Gridded posterior NBE, air-sea carbon exchanges, and uncertainties</u>	4° (latitude) x 5° (longitude)	Monthly	NetCDF	N/A
<u>Gridded prior NBE and air-sea carbon exchanges</u>	4° (latitude) x 5° (longitude)	Monthly and 3-hourly	NetCDF	N/A
<u>Gridded fossil fuel emissions</u>	4° (latitude) x 5° (longitude)	Monthly mean and hourly	NetCDF	N/A
<u>Region masks</u>	PFT and continents based 28 regions	N/A	csv	Figure 3 (section 2.4)
	Geographic -based 13 regions			
	TransCom regions			

1459

1460

1463  
1464

**Table: 6 The nine-year mean regional annual fluxes, uncertainties, and variability. Regions are based on the mask shown in Figure 5A (Figure 5.csv). Unit: GtC/year**

Region name (Figure4.csv)	Mean NBE	Uncertainty	Variability
<a href="#">NA shrubland</a>	<a href="#">-0.14</a>	<a href="#">0.02</a>	<a href="#">0.05</a>
<a href="#">NA needleleaf forest</a>	<a href="#">-0.22</a>	<a href="#">0.04</a>	<a href="#">0.06</a>
<a href="#">NA deciduous forest</a>	<a href="#">-0.2</a>	<a href="#">0.04</a>	<a href="#">0.07</a>
<a href="#">NA crop natural vegetation</a>	<a href="#">-0.41</a>	<a href="#">0.06</a>	<a href="#">0.18</a>
<a href="#">NA grassland</a>	<a href="#">-0.04</a>	<a href="#">0.03</a>	<a href="#">0.03</a>
<a href="#">NA savannah</a>	<a href="#">0.03</a>	<a href="#">0.02</a>	<a href="#">0.03</a>
<a href="#">Tropical South America (SA) evergreen broadleaf</a>	<a href="#">0.04</a>	<a href="#">0.1</a>	<a href="#">0.28</a>
<a href="#">SA savannah</a>	<a href="#">-0.09</a>	<a href="#">0.06</a>	<a href="#">0.18</a>
<a href="#">SA cropland</a>	<a href="#">-0.07</a>	<a href="#">0.03</a>	<a href="#">0.07</a>
<a href="#">SA shrubland</a>	<a href="#">-0.03</a>	<a href="#">0.02</a>	<a href="#">0.08</a>
<a href="#">Eurasia shrubland savanna</a>	<a href="#">-0.44</a>	<a href="#">0.07</a>	<a href="#">0.14</a>
<a href="#">Eurasia needleleaf forest</a>	<a href="#">-0.41</a>	<a href="#">0.07</a>	<a href="#">0.12</a>
<a href="#">Europe cropland</a>	<a href="#">-0.46</a>	<a href="#">0.09</a>	<a href="#">0.16</a>
<a href="#">Eurasia grassland</a>	<a href="#">0.02</a>	<a href="#">0.08</a>	<a href="#">0.13</a>
<a href="#">Asia cropland</a>	<a href="#">-0.37</a>	<a href="#">0.13</a>	<a href="#">0.08</a>
<a href="#">India</a>	<a href="#">0.14</a>	<a href="#">0.09</a>	<a href="#">0.14</a>
<a href="#">Tropical Asia savanna</a>	<a href="#">-0.12</a>	<a href="#">0.11</a>	<a href="#">0.08</a>
<a href="#">Tropical Asia evergreen broadleaf</a>	<a href="#">-0.09</a>	<a href="#">0.09</a>	<a href="#">0.12</a>
<a href="#">Australia (Aus) savannah grassland</a>	<a href="#">-0.11</a>	<a href="#">0.02</a>	<a href="#">0.09</a>
<a href="#">Aus shrubland</a>	<a href="#">-0.07</a>	<a href="#">0.01</a>	<a href="#">0.05</a>
<a href="#">Aus cropland</a>	<a href="#">-0.01</a>	<a href="#">0.01</a>	<a href="#">0.03</a>
<a href="#">African (Afr) northern shrubland</a>	<a href="#">0.04</a>	<a href="#">0.02</a>	<a href="#">0.03</a>
<a href="#">Afr grassland</a>	<a href="#">0.03</a>	<a href="#">0.01</a>	<a href="#">0.01</a>
<a href="#">Afr northern savanna</a>	<a href="#">0.54</a>	<a href="#">0.15</a>	<a href="#">0.49</a>
<a href="#">Afr southern savanna</a>	<a href="#">-0.27</a>	<a href="#">0.18</a>	<a href="#">0.33</a>
<a href="#">Afr evergreen broadleaf</a>	<a href="#">0.1</a>	<a href="#">0.07</a>	<a href="#">0.09</a>
<a href="#">Afr southern shrubland</a>	<a href="#">0.01</a>	<a href="#">0.01</a>	<a href="#">0.01</a>
<a href="#">Afr desert</a>	<a href="#">0.06</a>	<a href="#">0.01</a>	<a href="#">0.04</a>

1465  
1466

Deleted: Table: 5 List of the data products.  
Product

... [2]



1469

**Table: 7 Lists of data sources used in producing and evaluating posterior NBE product.**

Data name	Data Source
<a href="#">ECCO-Darwin ocean fluxes</a>	<a href="https://doi.org/10.25966/4v02-c391">https://doi.org/10.25966/4v02-c391</a>
<a href="#">CARDAMOM NBE and uncertainties</a>	<a href="https://doi.org/10.25966/4v02-c391">https://doi.org/10.25966/4v02-c391</a>
<a href="#">ODIAC</a>	<a href="http://db.cger.nies.go.jp/dataset/ODIAC/DL_odiac2019.html">http://db.cger.nies.go.jp/dataset/ODIAC/DL_odiac2019.html</a>
<a href="#">GOSAT b7.3</a>	<a href="https://oco2.gesdisc.eosdis.nasa.gov/data/GOSAT_TANSO_Level2/ACOS_L2S.7.3/">https://oco2.gesdisc.eosdis.nasa.gov/data/GOSAT_TANSO_Level2/ACOS_L2S.7.3/</a>
<a href="#">OCO-2 b9</a>	<a href="https://disc.gsfc.nasa.gov/datasets?page=1&amp;keywords=OCO-2">https://disc.gsfc.nasa.gov/datasets?page=1&amp;keywords=OCO-2</a>
<a href="#">ObsPack</a>	<a href="https://www.esrl.noaa.gov/gmd/ccgg/obspack/data.php">https://www.esrl.noaa.gov/gmd/ccgg/obspack/data.php</a>
<a href="#">ATom 1-4</a>	<a href="https://daac.ornl.gov/ATOM/guides/ATom_merge.html">https://daac.ornl.gov/ATOM/guides/ATom_merge.html</a>
<a href="#">HIPPO 3-5</a>	<a href="https://www.eol.ucar.edu/field_projects/hippo">https://www.eol.ucar.edu/field_projects/hippo</a>
<a href="#">INPE</a>	<a href="https://www.esrl.noaa.gov/gmd/ccgg/obspack/data.php?id=obspack_co2_1_INPE_RESTRICTED_v2.0_2018-11-13_and">https://www.esrl.noaa.gov/gmd/ccgg/obspack/data.php?id=obspack_co2_1_INPE_RESTRICTED_v2.0_2018-11-13_and</a>
<a href="#">FLUXSAT-GPP</a>	<a href="https://gs614-avdc1-pz.gsfc.nasa.gov/pub/tmp/FluxSat_GPP/">https://gs614-avdc1-pz.gsfc.nasa.gov/pub/tmp/FluxSat_GPP/</a>
<a href="#">NOAA MBL reference</a>	<a href="https://www.esrl.noaa.gov/gmd/ccgg/mb1/index.html">https://www.esrl.noaa.gov/gmd/ccgg/mb1/index.html</a>
<a href="#">CarbonTracker-Europe NBE</a>	<a href="https://www.carbontracker.eu/download.shtml">https://www.carbontracker.eu/download.shtml</a>
<a href="#">Jena CarbonScope NBE</a>	<a href="http://www.bgc-jena.mpg.de/CarboScope/?ID=s">http://www.bgc-jena.mpg.de/CarboScope/?ID=s</a>
<a href="#">CAMS NBE</a>	<a href="https://apps.ecmwf.int/datasets/data/cams-ghg-inversions/?date_month_slider=2009-12,2018-12&amp;param=co2&amp;datatype=ra&amp;version=v17r1&amp;frequency=mm&amp;quantity=surface_flux">https://apps.ecmwf.int/datasets/data/cams-ghg-inversions/?date_month_slider=2009-12,2018-12&amp;param=co2&amp;datatype=ra&amp;version=v17r1&amp;frequency=mm&amp;quantity=surface_flux</a>
<a href="#">Posterior NBE</a>	<a href="https://doi.org/10.25966/4v02-c391">https://doi.org/10.25966/4v02-c391</a>

1470

1471

1472

1473

1476

Deleted: ¶

Table: 6 The nine-year mean regional annual fluxes, uncertainties, and variability. Regions are based on the mask shown in Figure 5A (Figure 5.csv). Unit: GtC/year ¶  
Region name (Figure4.csv) ... [3]

Page 55: [1] Deleted	Liu, Junjie (US 329G)	9/30/20 10:47:00 AM
Page 57: [2] Deleted	Liu, Junjie (US 329G)	9/30/20 10:48:00 AM
Page 58: [3] Deleted	Liu, Junjie (US 329G)	9/30/20 10:49:00 AM